LIGHT SHEET REFLECTANCE MICROSCOPY

by

Christopher David Nguyen

A Thesis Submitted to the Faculty of the

DEPARTMENT OF OPTICAL SCIENCES

In Partial Fulfillment of the Requirements

For the Degree of

MASTER OF SCIENCE

In the Graduate College

THE UNIVERSITY OF ARIZONA

2019

THE UNIVERSITY OF ARIZONA
GRADUATE COLLEGE

As members of the Master's Committee, we certify that we have read the thesis prepared by Christopher David Nguyen, titled Light Sheet Reflectance Microscopy and recommend that it be accepted as fulfilling the dissertation requirement for the Master's Degree.

Dongkyun Kang — Date: 5/1/19

Arthur Gmitro — Date: 5/1/2019

Rongguang Liang — Date: 05/01/2019

[Committee Member Name] — Date: _____

Final approval and acceptance of this thesis is contingent upon the candidate's submission of the final copies of the thesis to the Graduate College.

I hereby certify that I have read this thesis prepared under my direction and recommend that it be accepted as fulfilling the Master's requirement.

Dongkyun Kang — Date: 5/1/19
Master's Thesis Committee Chair
Department of Optical Sciences and Biomedical Engineering

Table of Contents

List of Figures

Abstract

Many human diseases are diagnosed by the histopathological analysis of suspicious lesions where cellular morphological changes are examined at microscopic resolution. Reflectance confocal microscopy (RCM) and optical coherence tomography (OCT) are two optical imaging technologies that can visualize microscopic details of the tissue without having to remove or process the tissue. However, both RCM and OCT are generally expensive and have either limited field of view or low resolution. Light sheet microscopy, an imaging modality utilizing a thin sheet of light for illumination, can achieve comparable resolution compared to RCM while providing a field of view comparable to OCT. The light sheet microscope can be made at low cost by using a consumer-grade CMOS camera, an inexpensive light source such as an LED, and low-NA objective lenses. In this thesis, we have developed two simple light sheet microscopes with a goal of rapidly visualizing cellular details of the intact tissue either *in vivo* or *ex vivo*. The first utilized near-infrared illumination and the second utilized visible illumination. Preliminary imaging results showed that cellular details of the tissue can be visualized over a large field of view in both animal and human tissues.

Chapter 01: Introduction and Background

1.1 Skin Disease Diagnosis

According to the American Cancer Society, skin cancer is the most common form of cancer in the United States with an estimated 5.4 million cases each year of basal and squamous cell skin cancers. Both basal cell carcinoma and squamous cell carcinoma appear in the epidermis which is the uppermost layer of the skin as shown in Figure 1.01. It is split into 4 to 5 layers depending on the location on the body. They include, from the top most layer to the bottom, the stratum corneum, stratum lucidum, stratum granulosum, stratum spinosum, and the stratum basale. The relevant cellular features found in the epidermis include keratinocytes, melanocytes, and dermal papillae. Keratinocytes are the predominant types of cells in the epidermis, constituting 95% of the cells [1]. When they are located in the stratum basale, they are referred to as basal cells. Their primary function is to form a barrier against the environment such as providing protection against bacteria, viruses, parasites, radiation, and water loss. Melanocytes are found in the stratum basale and their function is to produce melanin which protects the skin from UV radiation. They constitute around 5% to 10% of the cells found in the stratum basale [1]. Dermal papillae are cellular features that actually originate from the dermis but extend into the epidermis to help provide support such as exchanging oxygen, nutrients, and waste products.

To image the cellular features of potential malignant sites on the skin, the tissue can either be removed through a biopsy for histopathological analysis or it can remain on the body and be imaged *in vivo*. Removing tissue for analysis places a financial and physical burden on the patient. The results, however, in the majority of biopsies turn out to be negative. Imaging *in vivo* can potentially remove these burdens with the added benefit of potentially acquiring results faster.

Current *in vivo* imaging techniques to diagnose skin cancer include reflectance confocal microscopy (RCM) and optical coherence tomography (OCT). RCM records en face or top-bottom images of the skin tissue with high lateral resolution for a field of view around 600µm by 600µm. The penetration depth is between 150µm to 200µm which is enough to image down to the top layer of the dermis. OCT records cross sections of the skin tissue with low resolution but for a large lateral field of view around 4mm to 10mm. The penetration depth achievable is around 2mm to 3mm which is enough to image down to the entire dermis. Both imaging modalities have advantages over the other; however, there lacks a device that images the skin *in vivo* with high resolution for a large field of view at low cost. This leads to a technique referred to as light sheet microscopy which has been primarily used for fluorescent imaging. However, for *ex vivo* fluorescent imaging, the staining is not always consistent and for *in vivo* imaging, the fluorescent dyes are not applicable for human patient imaging. Therefore, similar to confocal microscopy, the light sheet microscope will be used in reflectance mode. By using the light sheet microscope in reflectance mode, fresh tissue can be examined with little to no processing. As relatively low NA is used for the illumination and detection arms of the light sheet microscope, the microscope can achieve a large field of view while maintaining high resolution.

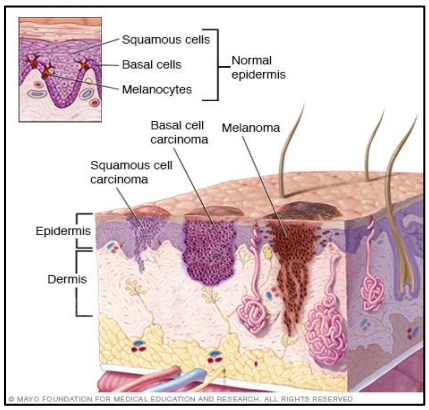

Figure 1.01 – Depiction of different forms of skin cancer that can appear in the epidermis including squamous cell carcinoma, basal cell carcinoma, and melanoma.

1.2 Confocal Microscopy

Confocal microscopy is an imaging modality which utilizes a pinhole gating or blocking method to reduce the signal from out-of-focus light. A schematic diagram is shown in Figure 1.02. In the illumination arm containing the source, the pinhole is used to generate a point source which is reflected by the beamsplitter and focused onto the sample by the lens. Due to tissue scattering, the sample before and after focus generates an out-of-focus signal which is collected by the lens. The blurred out-of-focus signal overlaps with the in-focus signal onto the detector which reduces the overall signal-to-noise ratio (SNR) of the tissue conjugate with the illumination point source. To prevent the out-of-focus signal from reaching the detector, a second pinhole is placed in front of the detector.

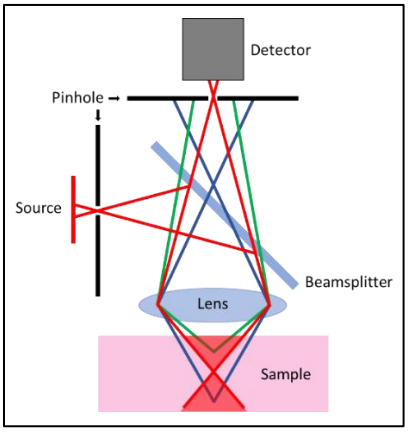

Figure 1.02 – Basic confocal microscope schematic. The red rays trace the optical path for the illumination and in-focus signal. The green and blue rays trace the out-of-focus signal.

With this configuration, the confocal microscope collects data on the sample point by point. Therefore, to generate an image of the sample, the point illumination is rastered across the sample in two dimensions to generate a 2D image. One configuration for the raster utilizes two mirrors to scan the beam in the x and y-dimensions across the sample. A second configuration utilizes two spinning disks referred to as Nipkow disks. A Nipkow disk is a disk with a pattern of pinholes stamped out at constant pitch [2]. The set of disks spin in conjunction to create multiple confocal

spots on the sample allowing faster large area scans. Both configurations are shown in Figure 1.03 below. To generate a 3D image, the device or sample is translated vertically while recording its position and the 2D images are stacked. The general size of the 2D images achievable by top-of-the-line commercial confocal devices is between 500µm x 500µm and 850µm x 850µm with a lateral resolution of around 1µm [3], [4]. However, these devices generally cost around $100,000 due to the expensive optics required to achieve the top-of-the-line resolution and field of view.

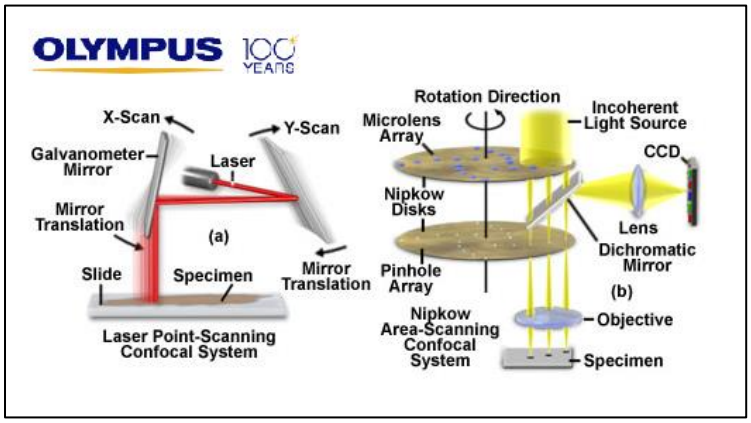

Figure 1.03 – Schematic from Olympus depicting a laser scanning and Nipkow area-scanning confocal microscope. The Nipkow disk rotates in conjunction to perform the pinhole gating.

A confocal microscope can be used in two modes depending on the desired image contrast. One mode is fluorescent mode based on fluorescence emission as shown in Figure 1.04. The chemical compound referred to as fluorophore is excited from its ground state to a higher energy state by absorbing an excitation photon which is generally provided by a laser. When it decays back down to its ground state, a photon which is the fluorescent signal is emitted with a lower energy or longer wavelength than the excitation photon. When these fluorophores bind to the biological markers they were designed for, the fluorescent signals can be associated to specific cellular features. An example is acridine orange which can bind to acidic vacuoles such as lysosomes and endosomes or DNA and RNA. For *ex vivo* studies, fluorescent mode is common due to its advantage of using stains to differentiate cellular features. However, for *in vivo* studies,

confocal microscopes are mainly used in reflectance mode. In reflectance mode, the signal is generated by the sample reflecting and scattering the illumination beam. The typical penetration depth achievable is between 150µm and 200µm depending on the imaging location [5].

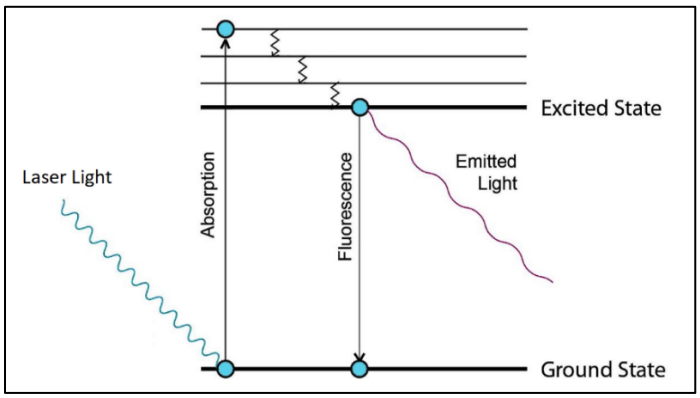

Figure 1.04 – Fluorescent emission diagram. Laser light is absorbed by the fluorophore and excites to a higher energy state. When decaying to the ground state, a fluorescent signal is generated.

One of the disadvantages of confocal microscopy is the collection of skin data en face for a small field of view. By collecting en face data, the various layers of the skin are hard to distinguish from one another which makes locating the dermoepidermal junction difficult. By having a small field of view, locating the general area to be image becomes difficult, prolonging the imaging time. A more desired form of data, therefore, are cross sections of the skin as it displays the tissue structure as a function of depth. Other disadvantages include the difficulty of aligning the pinholes and optics to achieve the optimal resolution and the inefficiency between illumination power and power collected as mentioned previously with Figure 1.02.

1.3 Optical Coherence Tomography

Optical coherence tomography (OCT) is an imaging modality based on low coherence interferometry to acquire data from individual planes of interest in the sample. A schematic diagram is shown in Figure 1.05. An OCT system, similar to most interferometric setups, consists

of a beamsplitter, reference mirror, and imaging optics. The source, however, is a low coherent source such as an LED. An application of low coherence tomography, similar to OCT, is white light interferometry. A white light source consists of wavelengths between 400nm to 700nm. To achieve white light fringes, the zeroth order fringes for all wavelengths formed from the interference between similar points generated by the reference and sample arm must intersect at the apparent location of where the reference and sample mirrors are coincident from the imaging system's point of view [6]. In other words, white light fringes are only observed when the mirrors are spaced equally from the beamsplitter. The same theory is applied to OCT in which only parts of the sample that correspond to the same optical path length as the reference arm interfere to generate an image.

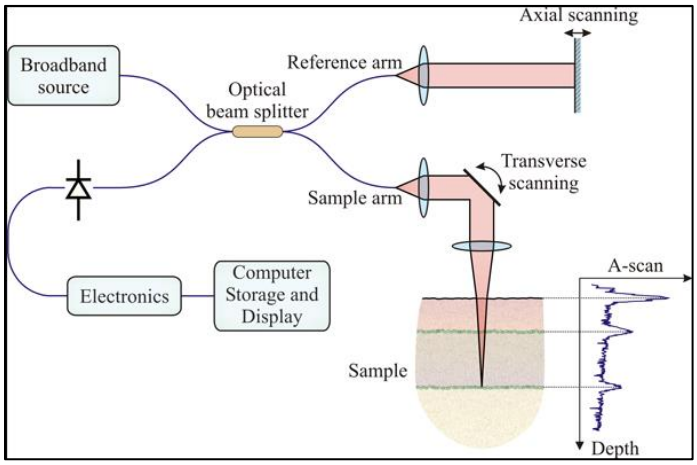

Figure 1.05 – Schematic diagram of time domain optical coherence tomography displaying A-scan data with a horizontal axis of intensity and vertical axis of depth.

Optical coherence tomography can be classified into two main categories which are time-domain OCT (TD-OCT) and frequency-domain OCT (FD-OCT). The first method developed was TD-OCT shown in Figure 1.05 above, which axially translates the reference mirror to image the sample at different depths. Lateral scanning is performed by deflecting the illumination beam using a scanning mirror. The resulting data is referred to as A-scans. By accumulating multiple A-scans,

a B-scan image can be generated which represents a cross-sectional view of the sample. Multiple B-scan images are used to generated volume data on the sample. The second category of OCT, FD-OCT as shown in Figure 1.06, is slowly replacing TD-OCT in the market.

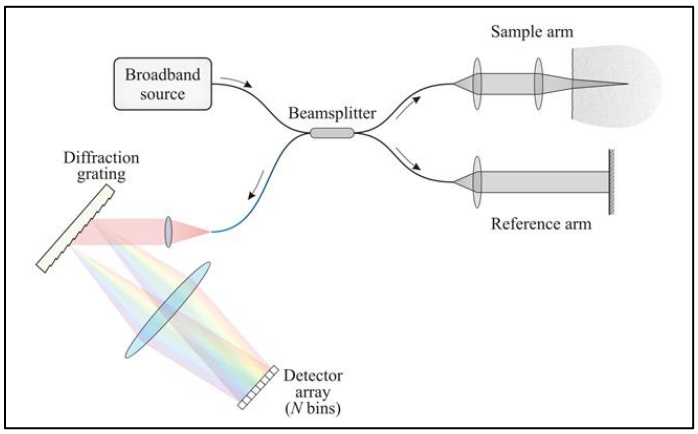

Figure 1.06 – Schematic diagram of Fourier domain optical coherence tomography. Consists of a diffraction grating and line detector to form a spectrometer.

One difference between the two categories is that the mirror in the reference arm for FD-OCT is stationary as translation isn't required to acquire images at different depths. When the sample is illuminated by a wavelength-swept or broadband source and collected by either a standard photodiode or spectrometer consisting of a grating and line detector respectively, the signal acquired is the integrated spectrum of the light source [7], [8]. Superimposed onto the signal are interference fringes with frequencies that correspond to the differences in pathlength or imaging depth in the sample [9]. By taking the Fourier transform of this signal, the reflectivity versus imaging depth is obtained. The benefits of using FD-OCT compared to TD-OCT is the decrease in acquisition time and an increase in detection sensitivity. The issue is the limited lateral resolution due to the illumination focus shift of different wavelengths caused by chromatic aberration. This can be mitigated by designing a system with a depth-of-field corresponding to the focus shift or using appropriate phase masks. The benefits and issues with using TD-OCT is the opposite of FD-

OCT. A TD-OCT system has the ability to shift focus to maintain the lateral resolution but it lacks a high acquisition speed [10].

The main advantage of using OCT compared to other imaging methods is the achievable penetration depth which is between 2mm and 3mm. For commercial OCT systems, the achievable lateral resolution and axial resolution is between 10µm and 15µm and between 12µm and 18µm respectively [11]. A typical horizontal field of view is 4mm to 16mm. With the given lateral resolution, individual cellular structures cannot be visualized; however, larger structures such as the dermal-epidermal junction in the skin can be visualized. However, in October 2018, a group published a journal article describing their line-field confocal OCT for high-resolution imaging of skin tumors *in vivo* [10]. The device is shown in Figure 1.07.

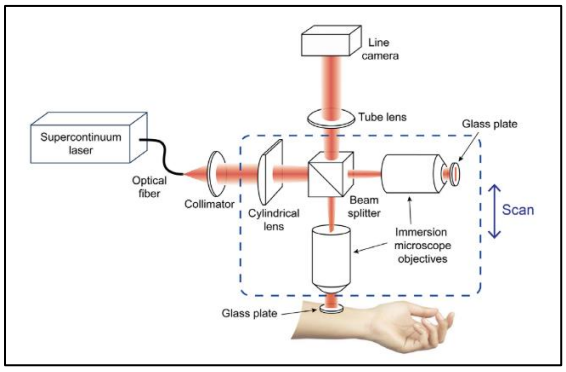

Figure 1.07 – Schematic diagram of line-field confocal OCT based on a Michelson interferometer in each arm. The source is a supercontinuum laser.

The achievable optical performance was an axial resolution of 1.15µm and a lateral resolution of 1.3µm which outperforms confocal microscopy in terms of axial resolution with similar lateral resolution. The lateral field of view was 1.2mm with a penetration depth of approximately 500µm. This OCT system outperforms many other *in vivo* imaging techniques; however, the use of a supercontinuum source is expected to set the device cost high, >$100,000, which limits its accessibility and therefore utility. Work is still required to reduce the cost of the system and its overall size but it is still an immense step towards advancing *in vivo* skin tissue imaging.

1.4 Light Sheet Microscopy

Light sheet microscopy is an imaging modality which utilizes a thin sheet illumination gating method to reduce the out-of-focus signal. The method was first introduced in 1902 to visualize gold molecules in colloidal gold solutions. By illuminating only a plane of the solution, the scattered signal collected had a significant increase in its SNR. Later development of light sheet microscopy eventually switched to utilizing it for fluorescence imaging, as similar to the confocal microscope, a light sheet microscope can be used in two modes depending on the desired illumination method. The first is fluorescent mode which collects the fluorescent signal from the parts of the sample marked with fluorescent probes. The main benefit of using a light sheet microscope in fluorescent mode compared to a confocal microscope is the amount of photobleaching. Confocal microscopy illuminates the sample before and after the point of interest, generating out-of-focus fluorescent signals that are blocked by the detection pinhole. The lifetime usability of the fluorescent markers in the out-of-focus regions decrease and eventually become permanently unable to fluoresce before being imaged. In conjunction with less photobleaching due to the sheet illumination, the degree of phototoxicity and therefore photodamage to the sample is decreased making light sheet microscopy desirable for long-term imaging studies. The second mode is reflectance mode which collects the reflected and backscattered signal from the sample.

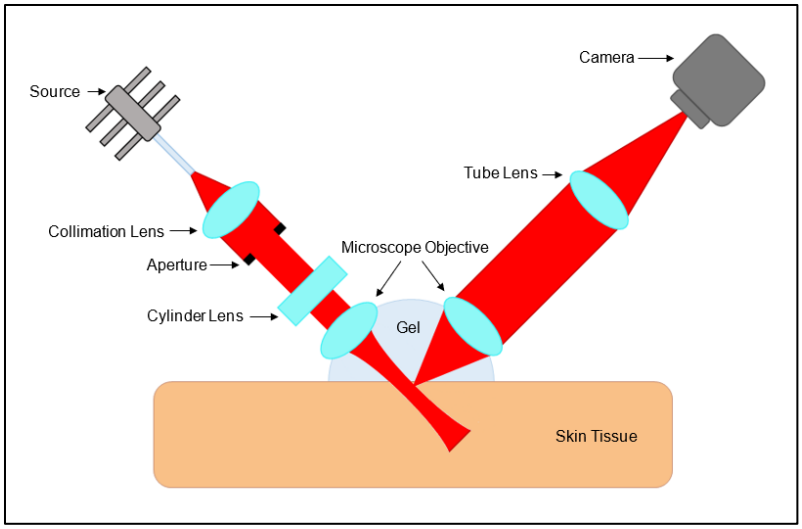

Figure 1.08 – Schematic diagram of a light sheet microscope. The sample is illuminated at 45 degrees by a fiber-based source. The immersion medium is ultrasound gel.

A schematic diagram of a simple light sheet microscope is shown in Figure 1.08 above. In the illumination arm, the source is focused into a thin sheet onto the sample by a cylinder lens, effectively only illuminating a slice of the sample at 45 degrees. The three important dimensions of the light sheet are the axial resolution, depth of focus, and width. The axial resolution or light sheet thickness determines how much signal overlaps in the detected image with the ideal being infinitely thin. With an infinitely thin light sheet, the out-of-focus signal would be close to zero resulting in the maximum SNR. The depth of focus determines the length of the sheet in which the thickness is considered to remain the same size. A longer depth of focus corresponds to a deeper penetration depth. When the sheet thickness expands, the SNR greatly decreases due to the amount of signal overlap. When the SNR decreases, the image blurs and cellular features are lost. The width of the light sheet determines the illumination field of view. Perpendicular to the optical axis of the illumination arm is the detection arm. The detection arm is aligned to place the focal plane coincident with the illuminated sample slice. By confining the illumination to a sheet and aligning the detection focal plane to the sheet, optical sectioning of the sample at 45 degrees is achieved as

only the slice signal is collected. By translating the sample or optical system, large area imaging is possible.

To improve the light sheet thickness or penetration depth, the illumination method can be modified to change either the method of light sheet generation, illumination wavelength, or illumination beam type. Modifying the light sheet generation may improve the axial resolution and increase the penetration depth. Generating the light sheet can be accomplished in two ways. The first is through the use of a cylindrical lens to focus the beam in one plane without affecting the orthogonal plane as shown in Figure 1.09.

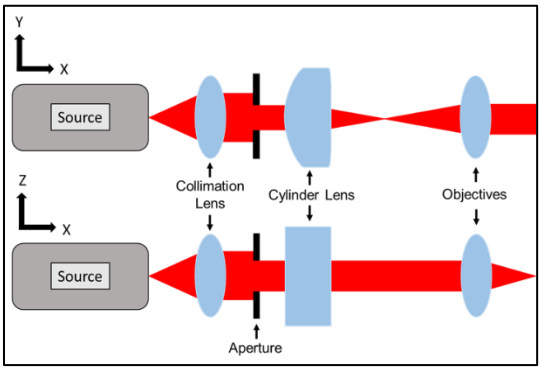

Figure 1.09 – Illumination configuration to generate the light sheet through a cylindrical lens. The sheet width is generated in the XY plane while the thickness is generated in the XZ plane.

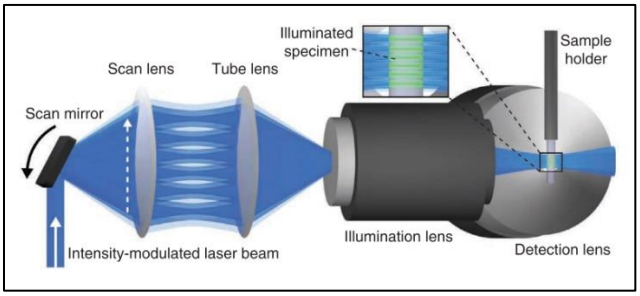

Figure 1.10 – Light sheet generation through a scanned beam. The beam is rastered across the same to create a 2D image similar to optical coherence tomography.

The second is to scan a beam in one direction, as shown in Figure 1.10, and stitch the resulting images together to create an effective large area image [12]. The main advantage of using a scanned light sheet is the dependence decoupling between the light sheet thickness and depth of

focus depicted by Equation 1.01 with ω_o representing the light sheet thickness and b representing the depth of focus [13].

$$b = \frac{2\pi\omega_o^2}{\lambda} \quad \textbf{(1.01)}$$

By using a scanned light sheet, the thickness can be reduced while still maintaining a long depth of focus. The disadvantage of this method is the expensive scanning mechanism as well as the reconstruction algorithm required to create a single cohesive image.

Modifying the illumination wavelength may increase the penetration depth. Basic microscopy techniques for biopsies utilize visible light after staining to visualize the sample features. However, for reflectance based *in vivo* techniques, the amount of absorption and scattering for visible light is relatively large compared to infrared radiation as shown in Figure 1.11.

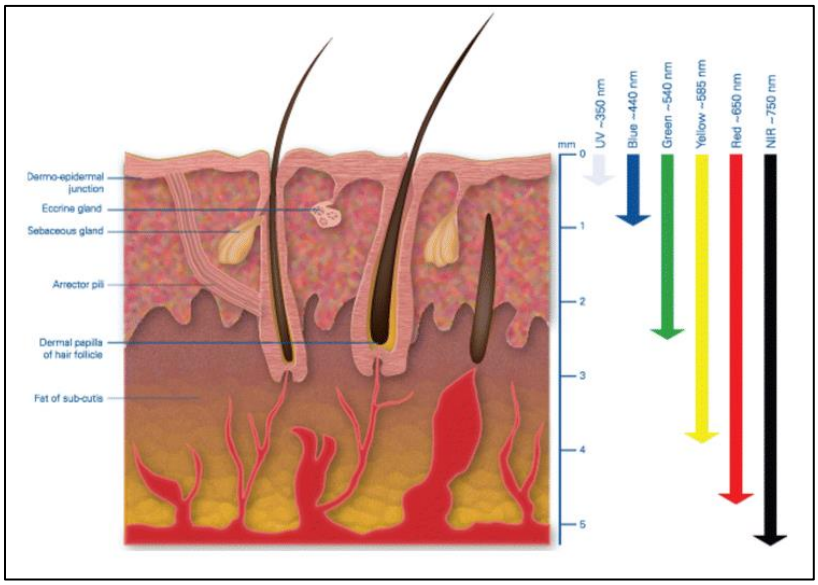

Figure 1.11 – Depiction of penetration depth of light into the skin as a function of wavelength. Labeled features are potential features that can scatter and absorb the light.

For absorption in the skin, the amount is dependent on the characteristics of the chromophores, or the part of a molecule responsible for color, present. For wavelengths shorter than 600nm, the dominant absorbing chromophores are present in melanin and hemoglobin. At longer wavelengths,

the amount of absorption decreases and the features become primarily dependent on scattering. The two types of scattering are Mie scattering and Rayleigh scattering. Mie scattering occurs for cellular structures larger or similar in size to the illumination wavelength such as melanosomes which have a diameter around 500nm. Rayleigh scattering occurs for smaller cellular structures such as small collagen fibrils in the uppermost layer of the dermis known as the papillary dermis [14], [15]. The trade-off then becomes gaining a larger penetration depth using infrared radiation but at the loss of any visible spectral information that may arise from the absorption of certain sample features.

Modifying the beam type may increase the penetration depth. The primary beam type in simple light sheet microscope systems is Gaussian. By modifying the beam type to either a Bessel or Airy beam which have interesting "self-healing" properties, the penetration depth for the light sheet microscope increases. Common methods of generating a Bessel beam involve interfering two plane waves which can be accomplished by either using an axicon or annular aperture placed at the front focal point of a lens. Both methods are shown in Figure 1.12 with the resulting beam profile represented by a Bessel function of the first kind.

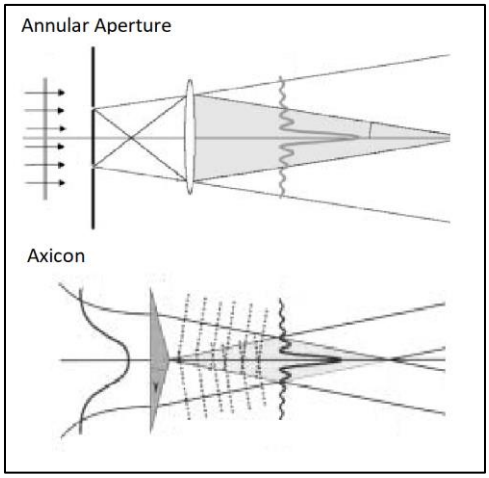

Figure 1.12 – Two different methods to generate a Bessel beam. The top places an annular aperture at the front focus of the lens. The bottom utilizes an axicon to interfere plane waves.

The increased penetration depth is due to the self-healing property of the Bessel beam as shown in Figure 1.13. As the beam is generated through interference, shadows that are casted by features that appear closer to the surface don't affect the illumination of deeper features.

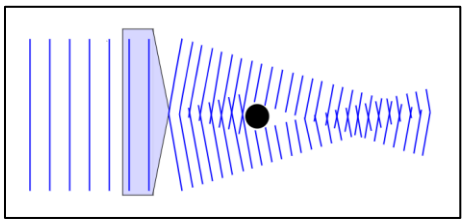

Figure 1.13 – Bessel beam generated by an axion. The object blocks the center of the beam; however, it reforms downstream allowing illumination of deeper sample features.

One method for generating an Airy beam is by inducing the coma aberration using a tilted cylindrical lens [16]. Other setups include the use of spatial light modulators, non-linear crystals, and phase masks [17]. A second interesting property of both these beams is that they do not spread out after being focused and propagated [18]. Disregarding the scattering of the sample, this property results in less overlapped signal as the axial resolution performance does not decrease from propagation. However, both these beams can only be used in a scanned system which have their disadvantages. Disadvantages specifically for Bessel beams include the axicon being expensive and the low power efficiency of an annular aperture design. The low power efficiency is due to most of the illuminating beam being blocked as the opening on the annular aperture must be similar in size to pinholes. The main disadvantage for Airy beams is the difficulty of generating a beam with high power and wavelength tunability while being low cost.

One of the disadvantages of using a light sheet microscope as mentioned are the shadow artefacts created from the single-direction illumination. The shadows are caused by sample features absorbing or scattering the illumination beam before it reaches the features downstream. A relatively simple solution is multiview imaging which involves rotating the sample, recording the individual images, and then fusing the images together.

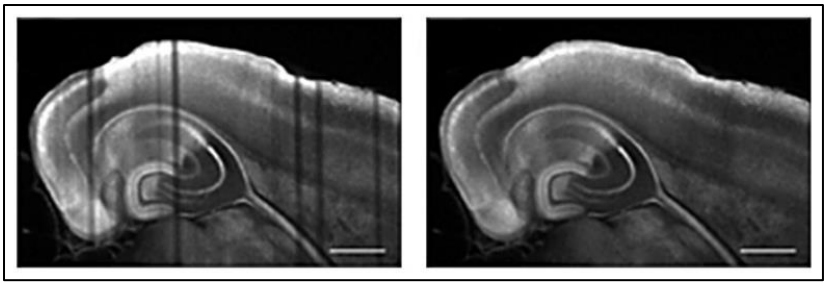

Figure 1.14 – Depiction of shadow artefacts removed from the image using multiview imaging. The sample was rotated at 90 degree increments to produce four images that were fused.

The signal lost from sample features downstream appear in the images from other angles resulting in a high-quality composite image as seen in Figure 1.14 above. However, the issues in using this method are the increase in acquisition time and data collected as well as potential motion artefacts from highly active samples. Additionally, the sample may not be uniformly illuminated in the composite image if the number of acquisition angles is limited. Acquiring multiple images to stack requires the sample to be stationary during rotation so that the same sample features are imaged in each frame. With each slice of the sample requiring 4-6 images depending on the division of imaging angles, imaging of live specimens becomes difficult [19]. As for *in vivo* imaging of skin tissue, this method isn't viable as the optical system or subject must rotate in the detection plane. An alternative solution is dual-sided illumination which involves illuminating the sample from two directions simultaneously. The second illumination objective is placed coincident with the optical axis of the first illumination objective. Sample features which have low signal downstream in single-direction illumination are now illuminated by the second objective. Current advanced methods utilizing dual-sided illumination include an additional detection objective placed coincident with the optical axis of the first detection objective as shown in Figure 1.15. The second detection objective allows image sampling from two directions, speeding up the acquisition process [20]. For *in vivo* imaging of skin tissue, this method isn't viable as the active area for imaging is too small.

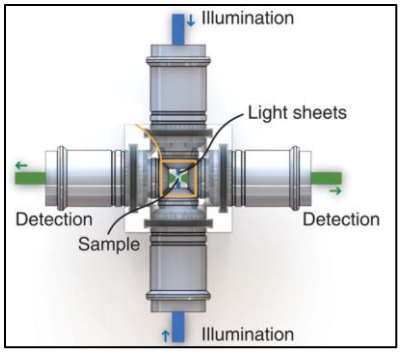

Figure 1.15 – Four objective selective plane illumination. The sample is illuminated from two directions and the signal is collected by two objectives for faster imaging speed.

1.5 Speckle

A major issue that many reflectance-based systems face is speckle noise. Speckle noise is caused by the interference between multiple random wavefronts of varying amplitude and phase. For reflectance-based microscope systems, the wavefronts are generated by the scattering of small sample features. Speckle noise is an issue due to its inherent property of having a SNR of 1. In other words, speckle noise contributes the same amount of signal as noise in the final image. The result is a random fluctuation in intensity which lowers the overall system resolution due to its influence on the base signal generated by relevant sample features. Images of speckle noise in confocal microscopy is shown below in Figure 1.16 [21].

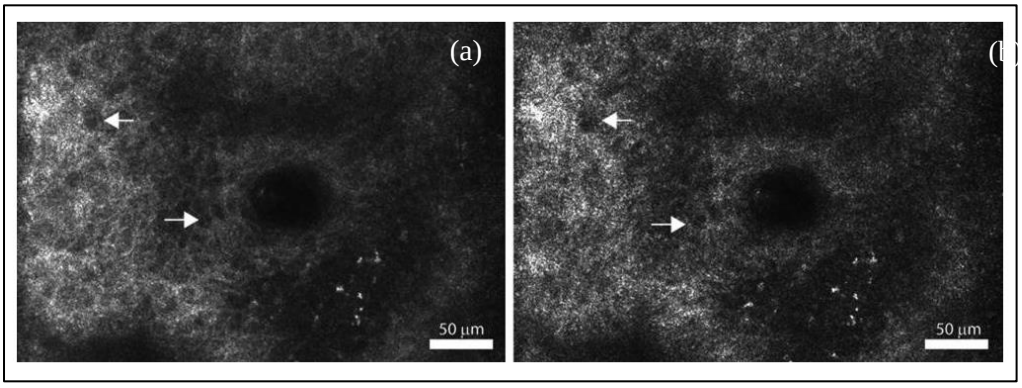

Figure 1.16 – Confocal images of skin tissue. (a) has less speckle than (b) due to increasing the pinhole size from a factor of 3.8 to 5.7 of the max resolution.

To reduce the amount of speckle noise, either the image can be manipulated to digitally reduce the speckle contrast, or the properties of the illumination can be modified. Speckle is characterized as high frequency noise in the image as it causes high frequency fluctuations in the image intensity. One method to digitally reduce the speckle contrast is to generate a simple low pass filter matrix and apply it to the image through a convolution. This method however results in the loss of contrast and edge sharpness for features similar in size to the maximum resolution. Sharp edges are considered high frequency features in an image as they provide sharp contrast for features that are different. By applying a low pass filter, the sharp edges are blurred to create a smoother transition between the bright and dark areas. As the edges are blurred, the resolution becomes worse [22]. Advanced methods to digitally correct speckle noise rely on statistical approaches to help characterize and mitigate the noise. An example of noise reduction in OCT using a curvelet-based K-SVD algorithm is shown in Figure 1.17 [23]. To help correctly model the noise in tissue, the features that cause speckle may be divided into three classes. The first are random features that constantly change such as blood cells flowing through veins for *in vivo* studies. The second are features that are random but predictable on large scales such as lobules in the liver for *ex vivo* studies. Lastly are spatially invariant structures such as organ surfaces or blood vessels [24]. However, if the model was generated incorrectly, the denoising process may introduce the creation of severe artefacts and the loss of resolution.

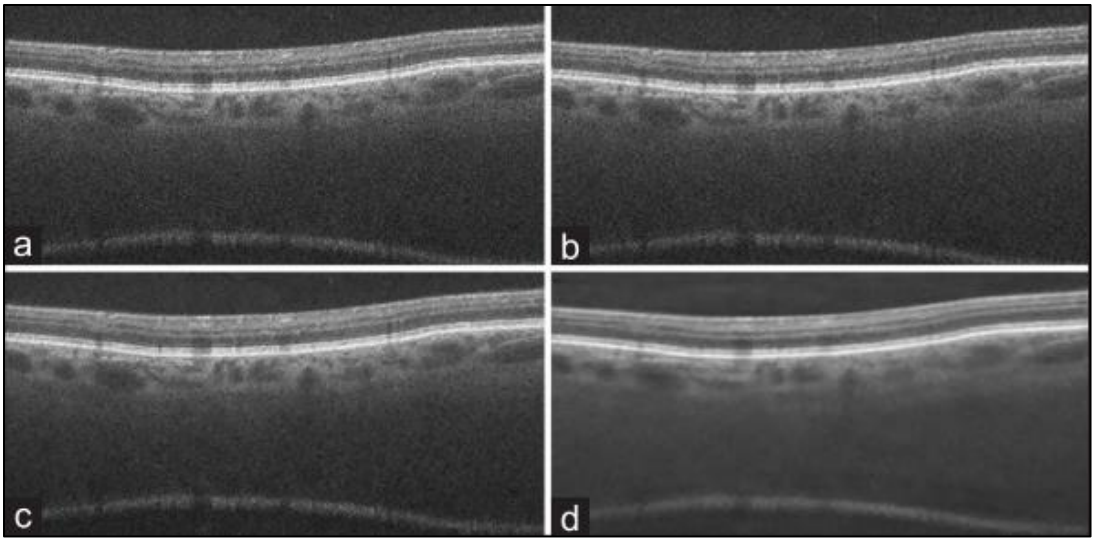

Figure 1.17 – Speckle reduction in OCT images using a K-SVD denoising algorithm. Images in order from "a" to "d" depicts the various steps through the algorithm.

Common methods to reduce the amount of speckle noise optically involve scrambling the spatial coherence of the source or increasing the source bandwidth to decrease the temporal coherence. Spatial coherence is a measurement of the wavefront phase uniformity. In other words, it measures the correlation of the phase between different locations in the propagation transverse to the direction of propagation. When the sample is illuminated, multiple wavefronts are generated due to scattering. If the source has a high spatial coherence, the phase of the wavefronts within close proximity have high correlation resulting in constructive interference known as speckle. A common method to reduce the spatial coherence is to pass the beam through a rotating or vibrating ground glass diffuser [25]. This method however has low power throughput even when using a lens to collect the diffused light. A second method is to illuminate the sample at multiple angles to generate multiple speckle patterns that ultimately reduce the speckle contrast during the detector integration time [26], [27]. Other methods include passing the light through a multi-mode optical fiber or a vibrating optical fiber. Temporal coherence is a measurement of the phase correlation between different points along the direction of propagation. In other words, it provides information

about the degree to which the source is monochromatic with a high temporal coherence corresponding to a more monochromatic source. To understand speckle contrast using Fourier methods, the visibility of two wavefronts interfering is derived to include the temporal coherence visibility factor as depicted in Equation 1.02 where $V(\tau)$ is the fringe visibility, I_1 and I_2 are the irradiance of the individual wavefronts, and $\mu^{\nu}(\tau)$ is the temporal coherence visibility factor.

$$V(\tau) = \frac{2\sqrt{I_1 I_2}}{I_1 + I_2}\mu^{\nu}(\tau) \quad \textbf{(1.02)}$$

The temporal coherence visibility factor is equal to the absolute value of the Fourier transform of the normalized source spectrum as depicted in Equation 1.03 where $f(\nu)$ is the normalized source spectrum. Using Fourier theory, a broad function in the spatial domain corresponds to a narrow function in the Fourier domain. If the source bandwidth is wide, the temporal coherence visibility factor is small resulting in low fringe visibility which manifests as a reduction in speckle contrast [28]. To calculate the actual speckle contrast, Equation 1.04 is used where C is the speckle contrast, σ_I is the standard deviation of the speckle pattern, and $\langle I \rangle$ is average speckle intensity.

$$\mu^{\nu}(\tau) = |\boldsymbol{F}\{f(\nu)\}| \quad \textbf{(1.03)}$$

$$C = \frac{\sigma_I}{\langle I \rangle} \quad \textbf{(1.04)}$$

For reflectance-based microscopy techniques, speckle is generally considered noise in the image. However, as speckle is created from the sample itself rather than the optical system, the speckle dynamics may provide pertinent information. The study of blood flow imaging exploits speckle dynamics to determine the location of blood vessels *in vivo* [29]. When multiple frames are acquired at the same location on the tissue, the flow of blood causes the speckle pattern to fluctuate and therefore generate a larger standard deviation in pixel value compared to the surrounding tissue. The results shown in Figure 1.18 demonstrates the use of speckle dynamics to

determine the location of blood vessels in a mouse brain *in vivo*. The mouse brain is illuminated by the source and the image collected is shown on the top right. Weighting the image using the standard deviation generates the image on the bottom right.

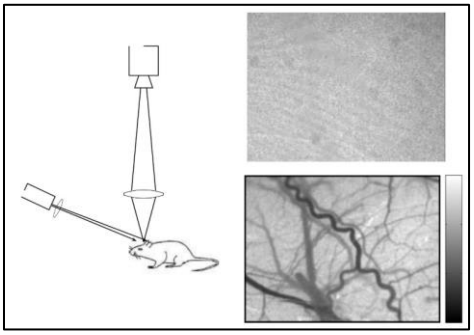

Figure 1.18 – Depiction of speckle dynamics used to determine the location of blood vessels in a mouse brain. Blood flow appears as a more uniform gray due to the speckle pattern averaging.

Chapter 02: Light Sheet Microscope with Infrared Illumination

2.1 Detection Design

One of the advantages of using a light sheet microscope is the relatively large achievable field of view due to the use of low numerical aperture (NA) objective lenses. However, due to the inherent inverse dependence between field of view and lateral resolution, the two parameters must be balanced to create a usable system. The lateral resolution was chosen to be between 1µm and 2µm to match basic confocal systems. Utilizing Equation 2.01 which calculates the resolution based on the Abbe diffraction limit for microscopes, the required NA was between 0.21 and 0.42 assuming a wavelength of 834nm which is explained in Section 2.2.

$$\text{Resolution} = \frac{1}{2}\frac{\lambda}{NA} \qquad \textbf{(2.01)}$$

To choose the objective lens for the system, the immersion medium must be considered. For *ex vivo* studies which place the sample in direct contact with the cover glass, oil immersion-based objectives are used. By using an immersion oil with a refractive index matching the front element of the objective lens and cover glass, the amount of spherical aberration is reduced compared to dry objective lenses as there is less refraction at each interface, and the full NA of the objective is filled. Similar for *in vivo* studies, using an immersion medium for imaging will increase the achievable resolution. However, as the viscosity of the oil-immersion medium is low, forming a droplet large enough to cover the supported field of view while completely immersing the first surface of the illumination and detection objective becomes complicated. For water-immersion objectives, a suitable alternative for the immersion medium is ultrasound gel which has a high enough viscosity to form the necessary droplet size and a refractive index close to water. Dry objectives are not used in both cases as immersion objectives achieve better resolution due to the increase in collection NA for the same size clear aperture. Based on these considerations, the

commercially available infinity-corrected objective lens chosen was a water immersion objective lens with a NA of 0.3 and focal length of 20mm. This results in, at best, a theoretical lateral resolution of 1.4µm assuming a wavelength of 834nm.

The desired object space field of view was chosen to be 2.5mm by 0.160mm. The full field of view of the objective will not be used for imaging due to the decrease in performance off-axis. The image width was therefore chosen to be 2.5mm. The 0.160mm height was chosen to match the illumination light sheet depth of focus which is later explained in Section 2.2. With the theoretical resolution and field of view known, the detector was chosen based on the number of pixels required to satisfy the Nyquist frequency. The Nyquist frequency is a sampling rate for continuous signals in which all the information is captured. In theory, by sampling at twice the highest frequency which is equivalent to half the smallest feature size, all the information is captured. Sampling at a lower frequency will result in aliasing artefacts appearing in the captured image, degrading the performance of the optical system as shown in Figure 2.01. To satisfy the Nyquist frequency, the minimum pixel dimension was 3596 pixels by 226 pixels which was calculated by dividing the field of view by half the theoretical lateral resolution. The chosen monochromatic detector had a pixel dimension of 4024 pixels by 3036 pixels with a pixel size of 1.85µm. The quantum efficiency was approximately 0.4 at the assumed 834nm wavelength.

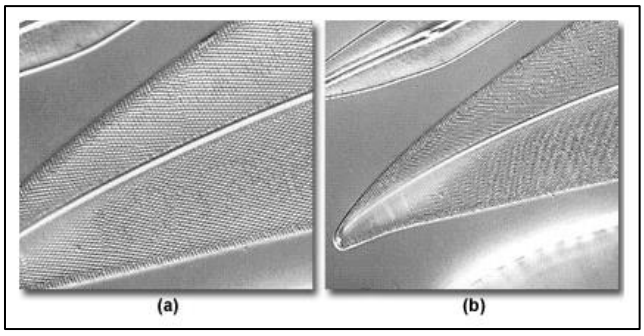

Figure 2.01 – (a) Sufficiently sampled image displaying the correct pattern. (b) Under-sampled image displaying aliasing artefacts.

To focus down the image onto the sensor with the correct size, the tube lens was chosen to provide the required magnification. The magnification was calculated by dividing the image space resolution by the object space resolution resulting in a required magnification of 2.66 or a tube lens focal length of 53.2mm. The image space resolution is equivalent to two times the pixel size as, based on the Nyquist frequency, two pixels are required to capture the smallest sample feature. Rather than design the tube lens, a CCTV camera lens was chosen due to its balanced performance versus cost when compared to designing and mounting a custom-made tube lens. Based on availability, a 50mm f/2.8 CCTV camera lens was chosen resulting in a magnification of 2.5 using Equation 2.02, changing the theoretical object space resolution based off the Nyquist frequency to 1.48µm. The theoretical field of view now supported by the sensor is 2.9mm by 2.2mm.

$$m_{eff} = -\frac{f_{tube}}{f_{objective}} \quad \textbf{(2.02)}$$

2.2 Illumination Design

The illumination wavelength for the light sheet microscope was chosen to be in the infrared spectrum. Based on previous works for other *in vivo* techniques, the infrared has less absorption in the skin compared to the visible. To decrease the speckle noise, a relatively large bandwidth fiber-based superluminescent laser diode (SLED) was used for illumination to reduce the temporal coherence. The central wavelength of the SLED was 834nm with a 3dB bandwidth of 44nm.

The three important dimensions to choose for the light sheet are the axial resolution, depth of focus, and width. However, before choosing the desired light sheet parameters, it was decided that the same low magnification objective lens used in the detection arm would be used to generate the light sheet as it would generate a high-quality beam with the desired axial resolution. The axial resolution of the system was chosen to be 5µm which is similar to the axial resolution of commercially-available RCM devices. Using Equation 2.03 where R_{axial} is the axial resolution,

the required NA to achieve the 5μm axial resolution was 0.083, resulting in a theoretical total depth of focus of 160μm using Equation 2.04. The beam diameter corresponding to the required NA was 2.508mm using Equation 2.05.

$$NA = \frac{\lambda}{2R_{axial}} \tag{2.03}$$

$$DOF = \frac{n\lambda}{NA^2} \tag{2.04}$$

$$D = 2f * \tan(\theta) = 2f * \tan\left(\text{asin}\left(\frac{NA}{n}\right)\right) \tag{2.05}$$

As the objective is infinity-corrected, the input beam is required to be collimated. Rearranging Equation 2.05, the required collimator focal length to achieve the 2.508 beam diameter was 12.475mm assuming that the source fiber NA was 0.1. With the SLED being fiber-based, the collimation was performed using a fiber-pigtailed aspheric collimator to achieve a high coupling efficiency. Based on the availability of the collimators for the design wavelength and that a larger beam diameter is preferred, an 18.45mm focal length fiber-pigtailed aspheric collimator was used resulting in a theoretical $1/e^2$ beam diameter of 4mm. A 1.71mm by 2.51mm square aperture was used to readjust the size of the beam. The width of the light sheet was chosen to be 2.5mm to match the desired detection object space field of view. To expand the beam from 1.71mm to 2.5mm, a 13.7mm cylinder is desired.

As the system was to be used for *in vivo* imaging, the maximum permissible exposure (MPE) onto the skin was calculated using the American National Standard for Safe Use of Lasers. It states that the MPE, in units of Watts/cm^2, for a wavelength between 0.4μm and 1.4μm is:

$$\text{MPE} = 0.2C_A \tag{2.06}$$

$$C_A = 10^{2(\lambda - 0.700)} \tag{2.07}$$

where C_A is the correction factor for wavelengths between 0.7µm and 1.05µm. Using the safety standard's 3.5mm limiting aperture diameter for long exposures, the MPE power was calculated to be 35.7mW which is above the 11mW maximum power output of the source. The source was therefore considered safe for skin exposure.

2.3 System Performance

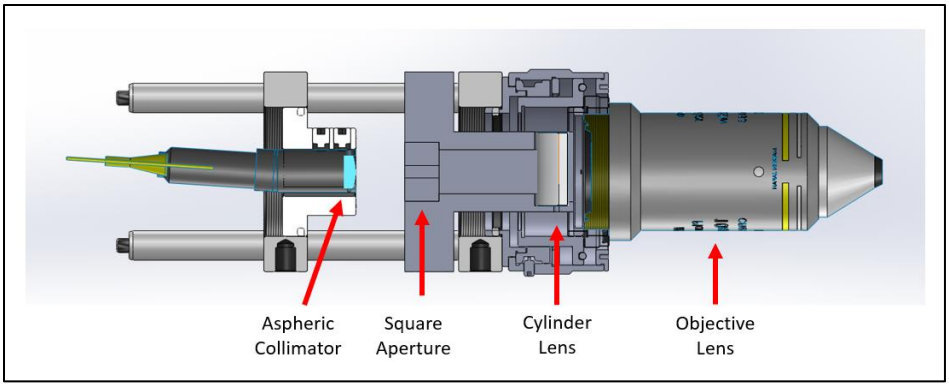

Figure 2.02 – CAD schematic displaying cross-section of the infrared illumination arm. The cross-section is in the XZ plane which matches the configuration in Figure 1.09.

The SLED source emitted directly into a fiber which was collimated using a fiber-pigtailed 18.45mm focal length aspheric lens as shown in Figure 2.02. The measured beam size exiting the aspheric lens was Gaussian with a $1/e^2$ radius of 4.1mm. To measure the axial resolution, a mirror was placed at the focus of the two objectives at an angle of 45 degrees with respect to the objectives. This reflected the beam exiting the illumination objective into the detection objective. The entire system was translated vertically to place the line illumination at the center of the detection field of view where the resolution was best. The axial resolution was measured by capturing an image of the line illumination and measuring the FWHM in the vertical direction. The result was an axial resolution of 5.9µm at the center of the field of view which was 18% larger than the theoretical. The magnification error was attributed to using a different illumination

wavelength rather than the design wavelength of the objective lens. To measure the depth of focus with the mirror, the entire system was translated vertically and the FWHM was measured at various vertical positions in the detection field of view. The vertical positions of the line illumination, labeled as units of pixel position in the image, were where the intensity was max. Using the conversion factor of 0.74μm/pixel from the detection arm, the light sheet maintained a thickness of less than 6.2μm for a length of 164μm as shown in Figure 2.03. The width of the light sheet, defined as the FWHM, was measured using the same image for the axial resolution, just in the perpendicular direction. The result was a width of 2.41mm.

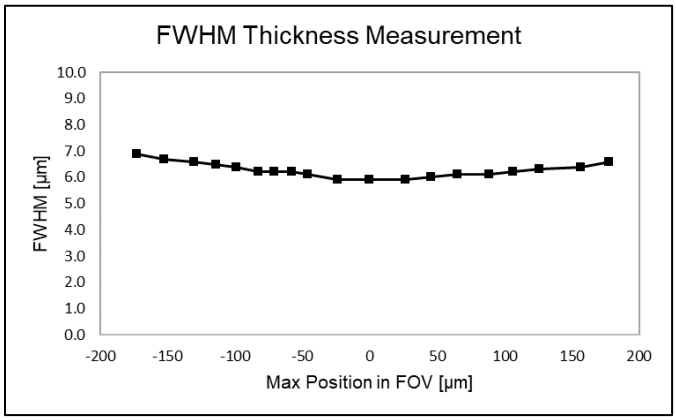

Figure 2.03 – Graph depicting the FWHM measurement of the light sheet thickness as a function of vertical position in the detection FOV.

To measure the lateral resolution, a USAF target was imaged through the system. To increase the confidence in the measured resolution, group 8 element 4 on the USAF target which corresponds to 362 lp/mm was imaged as shown in Figure 2.04. The contrast was 52%. The loss in resolution was attributed to using a different illumination wavelength rather than the design wavelength for both the objective and tube lens. The spread of a thin line represented by the "1" labeling group 8 element 1 on the target was measured to characterize the line spread function (LSF). In this case, the lateral resolution of the system was defined as the FWHM of the LSF. The result was a lateral resolution of 2.22μm.

To measure the field of view, the elements on the USAF target were used. Upon illuminating the thin line for the LSF, group 6 element 4 was illuminated. The thickness of each line in element 4 is 5.525µm which was represented by 8 pixels in the image. The total image width was 4024 pixels which results in a horizontal field of view of 2.8mm. This agrees with the theoretical field of view of 2.9mm. The completed system is shown below in Figure 2.05.

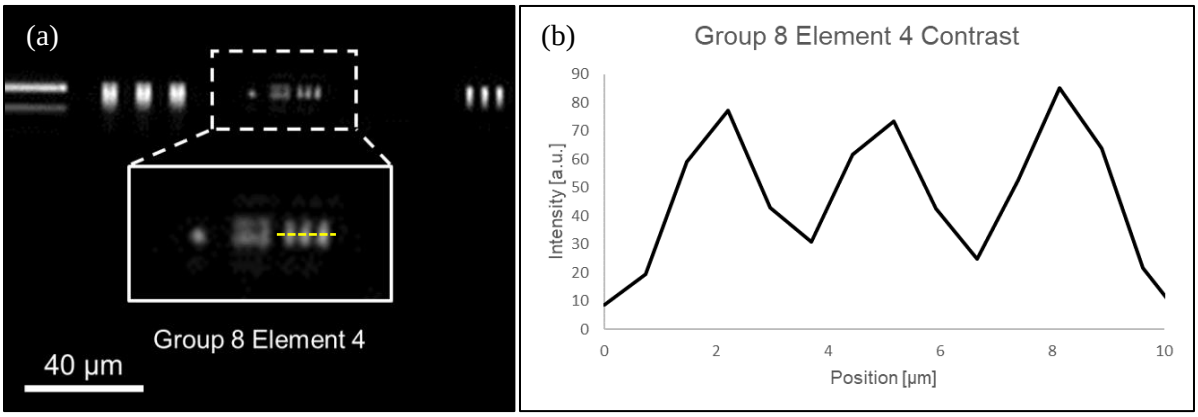

Figure 2.04 – (a) USAF target zoomed in to group 8 element 4. (b) Horizontal profile through the element following the dashed yellow line in (a). The contrast is 43%.

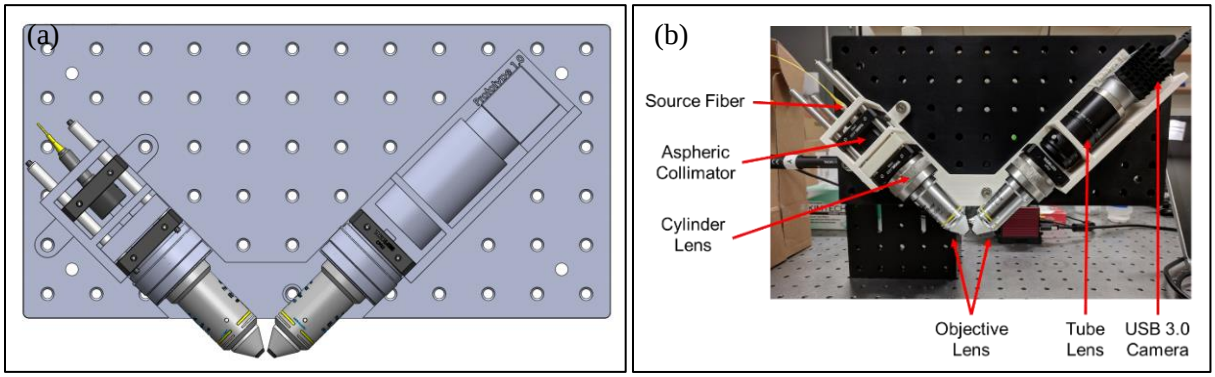

Figure 2.05 – (a) CAD model of the infrared light sheet microscope. (b) Real image of the microscope mounted onto an L-bracket.

Chapter 03: Light Sheet Microscope with Visible Light Illumination

The benefits of using near-infrared illumination is the increase in penetration depth due to less absorption and scattering. By using visible light, the penetration depth decreases but the resolution increases and spectral information may be obtained about the sample. The aim in pursuing a visible light sheet microscope is to determine whether the spectral information gained will help determine the identity of significant sample features.

3.1 Detection Design

Similar to infrared design, the lateral resolution was chosen to be between 1µm and 2µm which results in a required NA between 0.138 and 0.275. However, the lowest NA water-immersion objective lens available was the same one used for the infrared design. Assuming a center wavelength of 550nm which is later explained in Section 3.2, this results in a maximum theoretical lateral resolution of 0.920µm.

To keep the design of the visible light sheet microscope similar to the infrared design, the color version of the monochromatic camera was used as the sensor. The pixel dimensions were 4024 pixels by 3036 pixels with a pixel size of 1.85µm. To focus the image down onto the sensor with the correct size, the tube lens focal length was calculated to be 80.7mm to provide a magnification of 4.04. Based on the availability of CCTV camera lenses, a 75mm f/3.9 camera lens was chosen resulting in a magnification of 3.75 and a theoretical object space resolution of 0.987µm. The theoretical field of view now supported by the sensor is 2.0mm by 1.5mm.

3.2 Illumination Design

The source used to provide the visible illumination was a supercontinuum laser with a power density shown in Figure 3.01. The infrared power was absorbed using a neutral density filter with an optical density of 6 between 0.8µm and 2.6µm. A reflective short-pass filter was used to remove wavelengths above 650nm. As seen in the graph, the power output in the 400nm range is significantly lower than the power output above 500nm. Digitally enhancing the signal in the blue channel will not improve the results as the low power output results in a poor SNR. Enhancing a poor SNR will increase the amount of noise and artificially introduce artefacts that may be misconstrued as significant. Therefore, the only channels that will be considered in the results are the red and green channels.

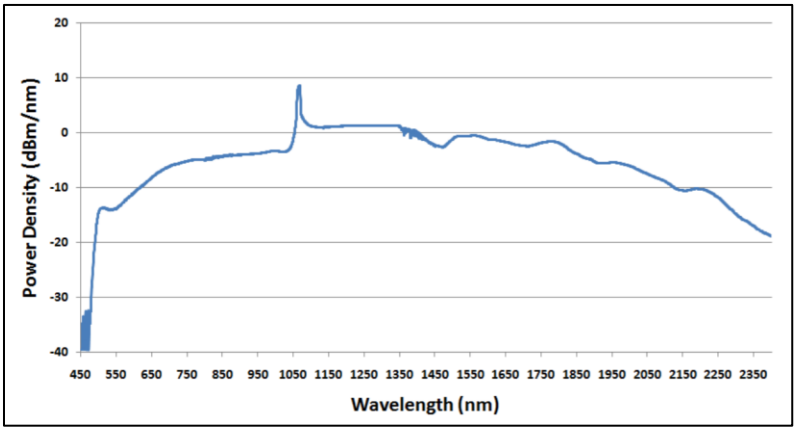

Figure 3.01 – Power density graph of the supercontinuum source. The power output below 500nm is significantly lower compared to the other wavelengths and will therefore be ignored.

To collimate the source, multiple commercial-off-the-shelf collimators were analyzed for beam size versus propagation distance. One of the considerations for choosing the collimator is the resulting beam size and the availability of the required cylinder lens to expand the beam to illuminate the desired detection field of view. The collimator with the best performance for the red and green channels was a triplet collimator with a focal length of 12mm at a wavelength of 543nm. The beam width versus propagation distance is shown in Figure 3.02 for 543nm and 656nm after

passing through the beam expander consisting of the cylinder lens, chosen in conjunction with the collimator, and the objective lens. The maximum beam propagation distance is the objective working distance of 3.5mm resulting in a theoretical beam width of 2.2mm and 2.7mm for the green and red channel respectively. This was calculated by applying a fit to the beam width versus propagation distance curve.

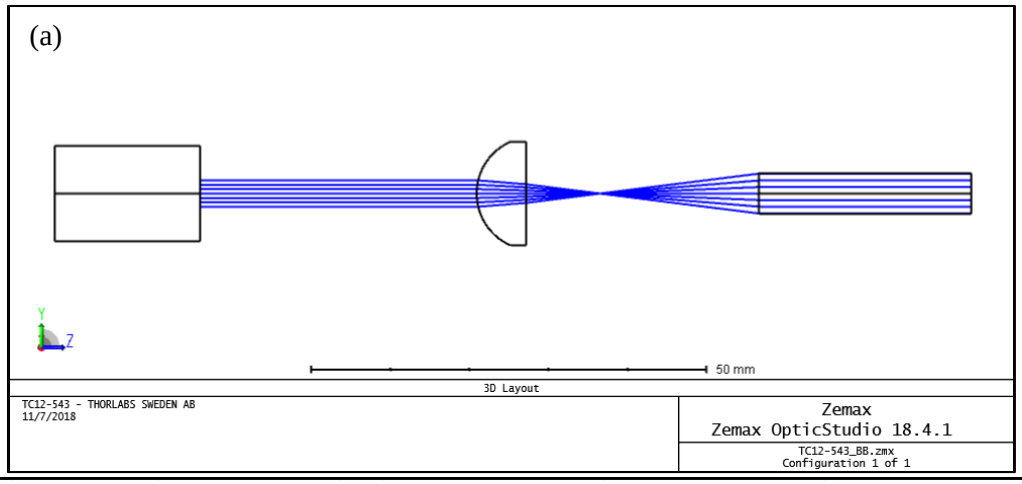

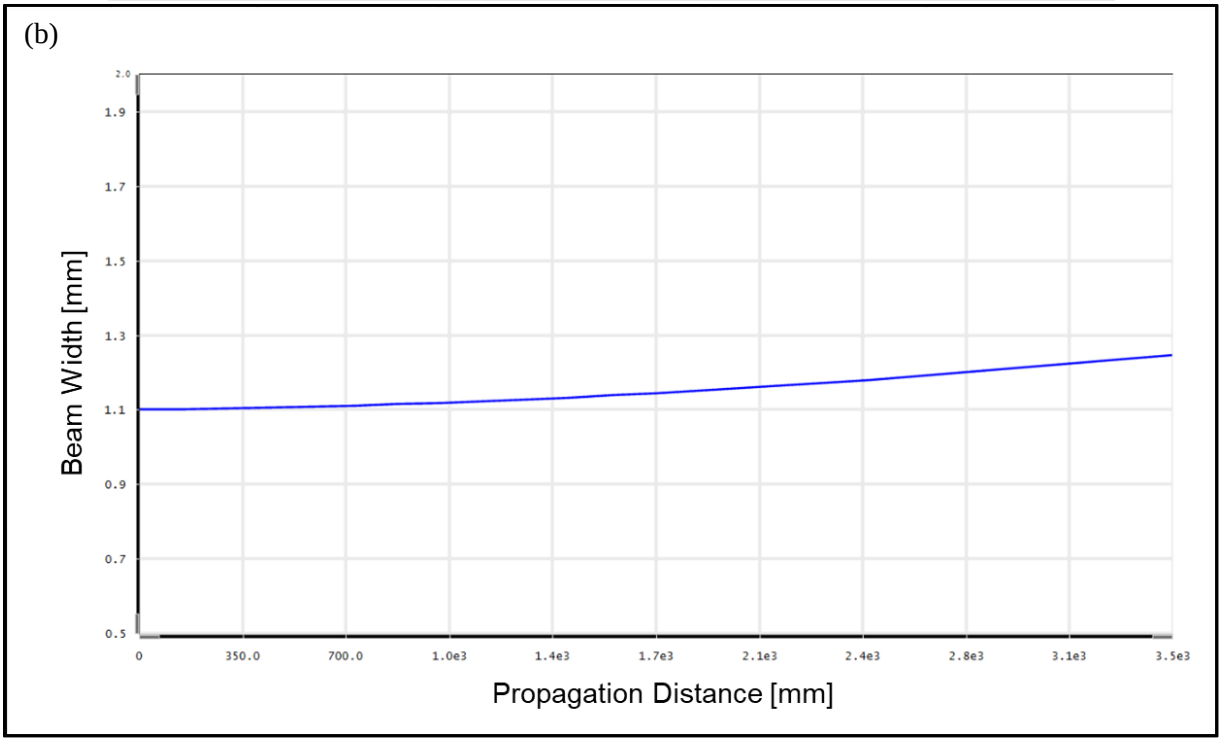

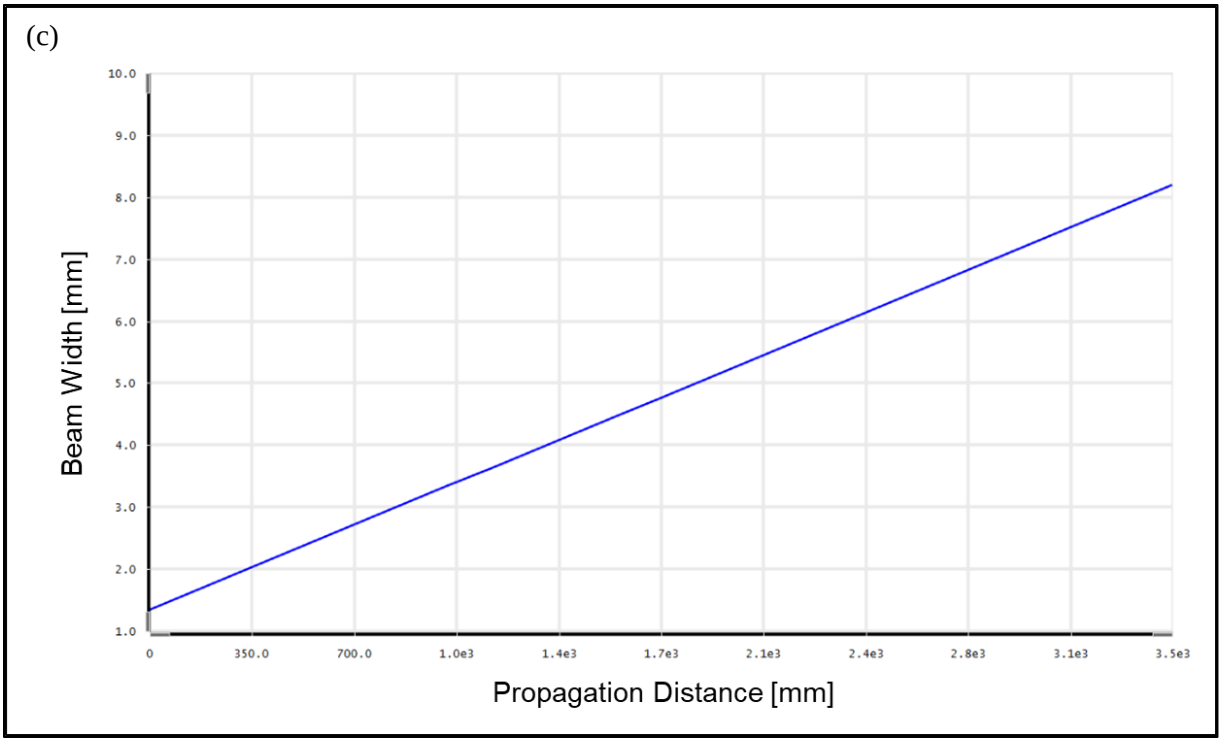

Figure 3.02 – (a) Lens schematic for analysis including black box for triplet. (b) Collimator performance for 543nm. (c) Collimator performance for 656nm.

To shrink the light sheet width from 2.2mm to 2mm, the required cylinder lens focal length was 22mm. The available cylinder lens had a focal length of 22.2mm resulting in a theoretical beam output of 1.98mm. The axial resolution was set to 3.76µm to utilize the full $1/e^2$ output beam from the collimator which was 2.2mm. The required NA was 0.073 resulting in a theoretical depth of focus of 137µm. A cross section of the illumination arm is shown in Figure 3.03 below.

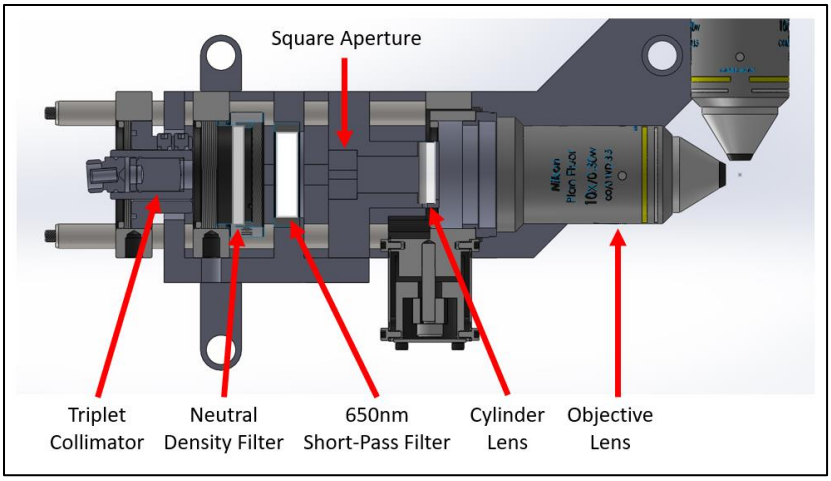

Figure 3.03 - CAD schematic displaying cross-section of the visible light illumination arm. The cross-section is in the XZ plane which matches the configuration in Figure 1.09.

Similar to the infrared prototype, the MPE onto the skin was calculated using the American National Standard for Safe User of Lasers due to concerns of skin damage. However, the correction factor for wavelengths between 0.4µm and 0.7µm was changed to $C_A = 1.0$. The limiting 3.5mm aperture stayed the same. The result was an MPE power of 19.2mW. To calculate the power output of the laser, the source parameters required are the applicable spectral bandwidth and the power spectral density. The spectral bandwidth used for the calculation was 470nm to 650nm and the spectral density was assumed to be -10dBm/nm or 0.1mW/nm. The actual spectral density fluctuates across the spectral bandwidth but was assumed to be the maximum value to calculate the maximum theoretical power output. The result was a theoretical power output of 18mW. The actual power output measured using a power meter was between 4.5mW and 5.5mW assuming a wavelength of 550nm. As the actual power output was less than the MPE power, the source was considered safe for skin exposure. The large power loss was attributed to a low coupling efficiency using the FC/APC fiber coupler.

3.3 System Performance

The theoretical and measured spectrum of the supercontinuum source is shown in Figure 3.04. The general shape of the spectrum between 500nm and 650nm match one another. Past 650nm, the short-pass filter reflects the light causing the normalized intensity to drop to zero.

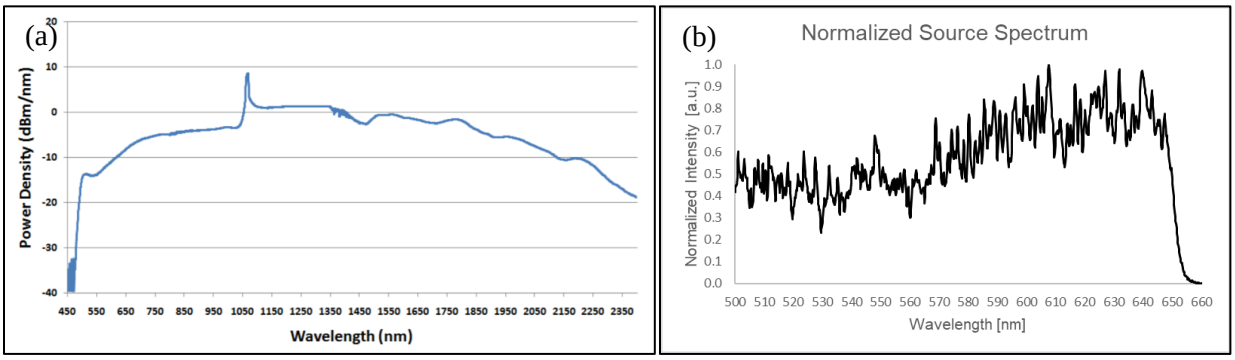

Figure 3.04 – (a) Theoretical spectrum of supercontinuum source. (b) Measured normalized spectrum of supercontinuum source.

The measured beam size exiting the collimator had a FWHM of 2.8mm. To measure the axial resolution and depth of focus, the same method as the infrared design was used as shown in Figure 3.06. For both measurements, the green channel was used due to the Bayer filter of the camera and the fact that green is the center wavelength for visible light which was the main wavelength bandwidth of the objective. The result was an axial resolution of 4.4µm at the center of the field of view. As for the depth of focus, the sheet maintained a thickness of less than 4.7µm for a length of 149µm as shown in Figure 3.05. The width of the light sheet was measured to be 1.7mm.

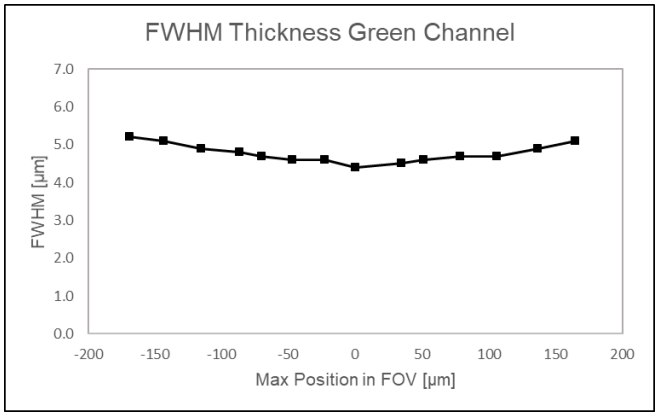

Figure 3.05 – Graph depicting the FWHM measurement of the light sheet thickness as a function of vertical position in the detection FOV.

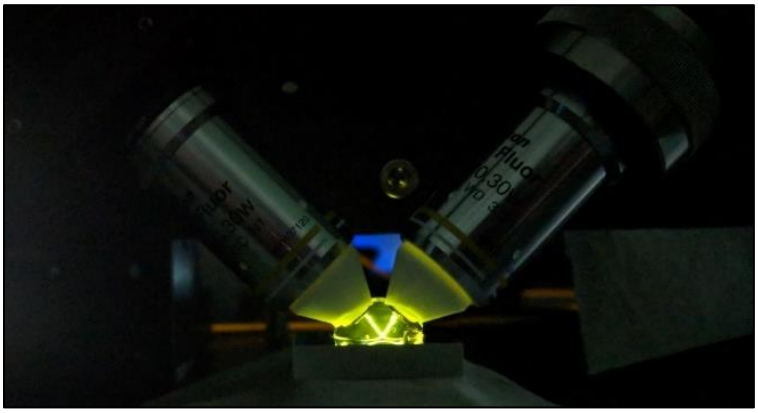

Figure 3.06 – Image taken during axial resolution and beam width testing. Driving current of the source was lowered from the maximum to primarily output the green wavelength.

To measure the lateral resolution, a thin line on the USAF target was imaged through the system. As the sensor differentiates the red and green channels, the lateral resolution was recorded for both channels. To increase the confidence in the measured resolution, group 9 element 1 on the USAF target which corresponds to 512 lp/mm was imaged as shown in Figure 3.07. The contrast was 45%. The lateral resolution, defined as the FWHM of the LSF, was 2.3µm and 1.7µm for the red and green channels respectively. The red channel's lateral resolution was larger than the infrared as the visible illumination system was aligned to have the green channel at best focus.

To measure the field of view, group 6 element 6 on the USAF target was used. The result was a horizontal field of view of 1.9mm which agrees with the 2.0mm theoretical field of view. The completed system is shown in Figure 3.09 below.

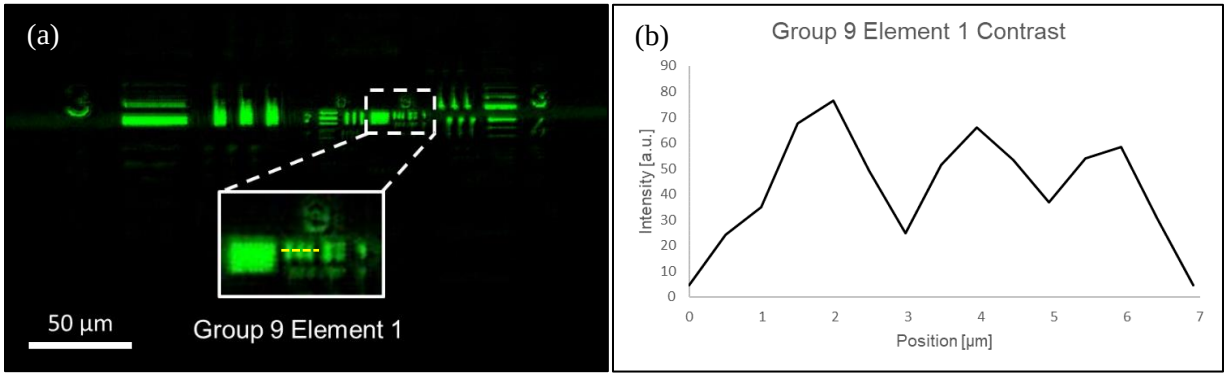

Figure 3.07 – (a) USAF target zoomed in to group 9 element 1. (b) Horizontal profile through the element following the dashed yellow line in (a). The contrast is 45%.

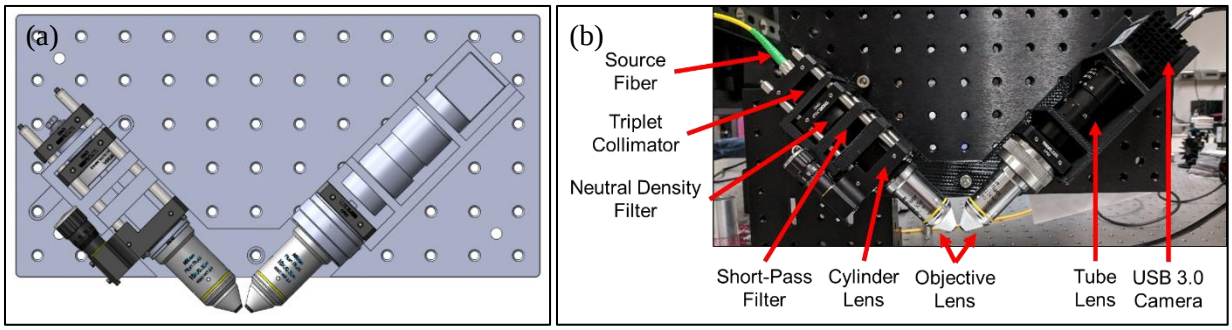

Figure 3.08 – (a) CAD model of the visible light sheet microscope. (b) Real image of the microscope mounted onto an L-bracket.

Chapter 04: Imaging Results

4.1 Processing Data

The basic schematic for the light sheet microscope places the top layer of the sample at a 45-degree angle relative to the optical axis of the detection arm. Vice versa, the focal plane of the detection arm is at an angle of 45-degree relative to the top layer of the sample. The data collected therefore are diagonal slices of the sample that follow the illumination path through the sample as shown in Figure 4.01. The issue with this is that even though the data is physically representing a diagonal, it is being recorded and therefore displayed as flat images on the screen. If an en face view is desired, directly resampling the data from the top will result in the wrong dimensions.

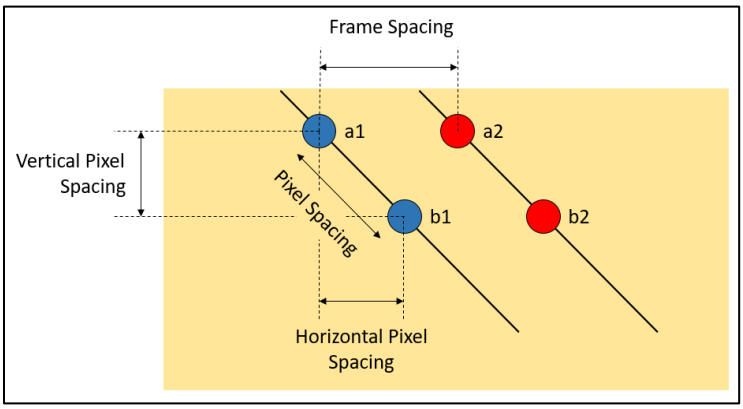

Figure 4.01 – Representation of data collection scheme. Different colored circles represent different frames which are in the plane perpendicular to the page.

Figure 4.02 – Pictorial representation of resampling data from the left to match the configuration in the Figure 4.01. Similar numbers are associated to their original raw frames.

To begin fixing the data, the volume matrix was resampled from the left to represent the configuration shown above in Figure 4.02. As the data is physically representing a diagonal, an

affine transformation was applied to the resampled volume matrix to shear the data as shown with the equations in Equation 4.01.

$$\text{Shear Matrix in X-Direction: } \begin{bmatrix} x' \\ y' \\ z' \\ 1 \end{bmatrix} = \begin{bmatrix} 1 & m & 0 & 0 \\ 0 & 1 & 0 & 0 \\ 0 & 0 & 1 & 0 \\ 0 & 0 & 0 & 1 \end{bmatrix} \begin{bmatrix} x \\ y \\ z \\ 1 \end{bmatrix} \rightarrow \begin{matrix} x' = x + my \\ y' = y \\ z' = z \end{matrix} \quad \textbf{(4.01)}$$

To calculate the shear factor "m", a conversion factor between pixel size and the physical dimension is required. The physical dimension that is known is the frame spacing which was set during the image acquisition process as the quotient between the total scan range and the number of desired frames. The motor speed was set as the product between the frame spacing and image acquisition speed. As the data were resampled from the left, each pixel spacing is equivalent to the frame spacing which gives the conversion factor in units of length per pixel. The shear factor is calculated by dividing the physical horizontal shift by the conversion factor. To calculate the required horizontal shift, the horizontal spacing, as shown in Figure 4.01, is multiplied by the cosine of the illumination angle which is 45 degrees. The last step involves a vertical compression or elongation of the data to have a one-to-one ratio between the vertical and horizontal dimensions. Currently, the vertical dimension has a pixel spacing of one which is set as the frame spacing. The actual vertical spacing is the frame spacing multiplied by the cosine of the illumination angle. The compression or elongation amount is therefore equivalent to the value of the horizontal shift. This is summarized pictorially in Figure 4.03. One thing to note is that when the volume matrix is resampled to represent en face imaging, each frame moves diagonally down the sample. The resulting matrix is therefore a parallelogram as shown in Figure 4.03. If en face imaging is desired that moves directly down, the ends of the matrix may be removed to only display the data in the rectangle.

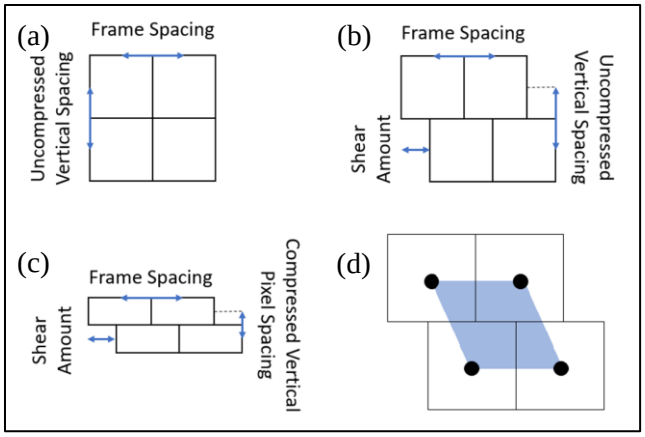

Figure 4.03 – (a) Matrix representing the volume matrix after resampling the raw data from the left. (b) Shearing the matrix to represent the configuration in Figure 4.01. (c) Compressing the data in the vertical direction to match the horizontal direction. (d) Resampled data represents a parallelogram represented by the shape shaded in blue.

One of the issues with imaging skin tissue *in vivo* is the movement of the subject. To collect volumetric data, the sample should ideally only translate laterally at a consistent velocity throughout the scan. When the subject moves laterally, the physical spacing between frames is erratic which makes the matrix transformation result in data that isn't representative of the sample. High-speed imaging along with fast translation stages are therefore desired to image the subject with the best accuracy. However, for large area scanning with the light sheet microscope, the large sensor size limits the image acquisition speed. Therefore, to mitigate any noise artefacts that may arise from random vertical movements, image registration algorithms may be applied to smooth the transition between image frames. If multiple frames are taken of the same sample plane, image registration may be applied to improve stability for speckle dynamic imaging to visualize areas of blood flow.

4.2 Light Sheet Microscope with Infrared Illumination Results

4.2.1 Plant Images

Before using the infrared light sheet microscope to collect data of the skin, the system was used to image plants to determine whether the system could visualize larger structures similar to OCT. The plant that was imaged was of a cucumber which was theorized to display a large density of cell walls. The results are shown below in Figure 4.04. The images are comparable to OCT images of cucumbers which display similar structures as shown in Figure 4.05 [30].

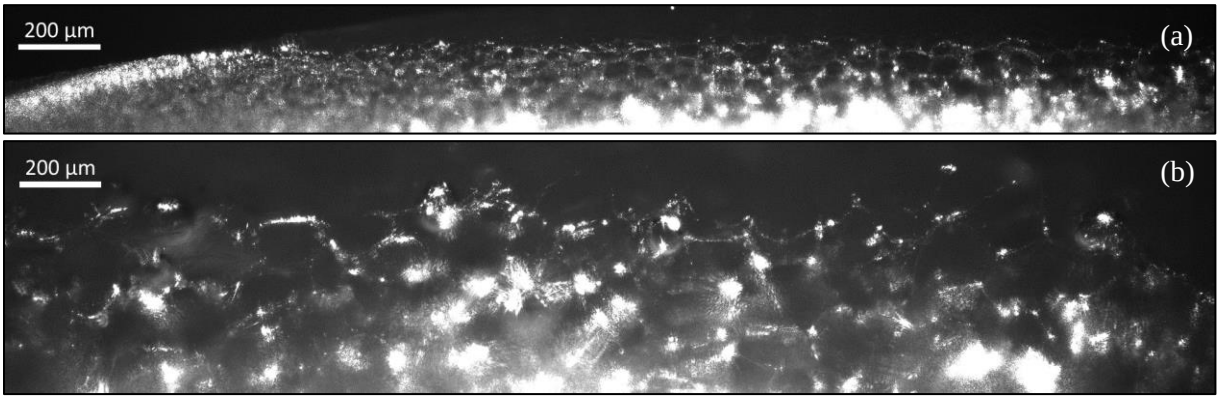

Figure 4.04 – Image of cucumber cells. (a) Near the edge. (b) Close to the center.

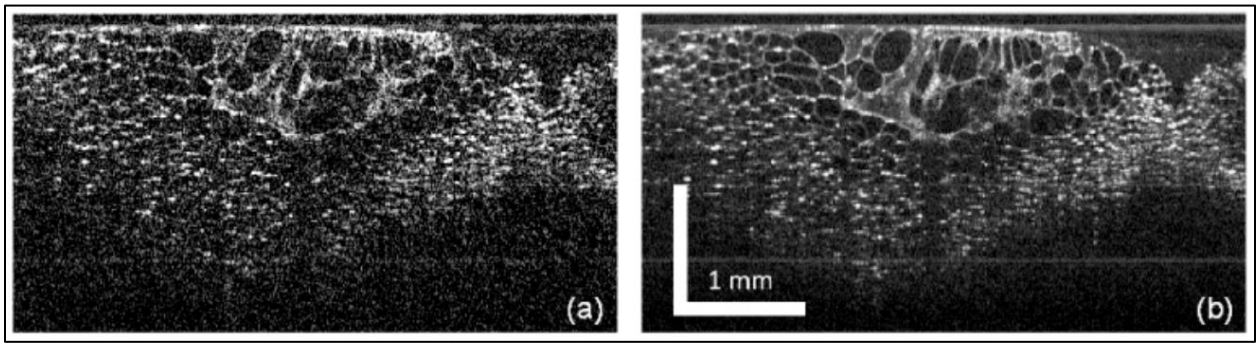

Figure 4.05 – Image of cucumbers taken with FD-OCT. The system consisted of a 1050nm Fourier-domain mode-locked laser with a tapered amplifier gain medium.

4.2.2 Animal Tissue Images

After imaging the plant cells, the system was used to image anime tissue cells *ex vivo*. The animal tissue that was imaged was swine kidney as it contains well known tissue structures. The sample was placed at the focus of the system and images were acquired at the max frames per second while the system translated horizontally across the sample with the desired motor speed. An individual frame of the results is shown in Figure 4.06(a). The relevant acquisition parameters were an acquisition speed of 30 frames per second, a motor speed of 8µm per second, and a total scan range of 960µm. The sample was illuminated by 0.9mW for an exposure time of 7.0ms. The video acquired was then processed using the method in Section 4.1 and the results are shown in Figure 4.06(b). The shear factor and compression amount were -0.0654 and 6.54% respectively.

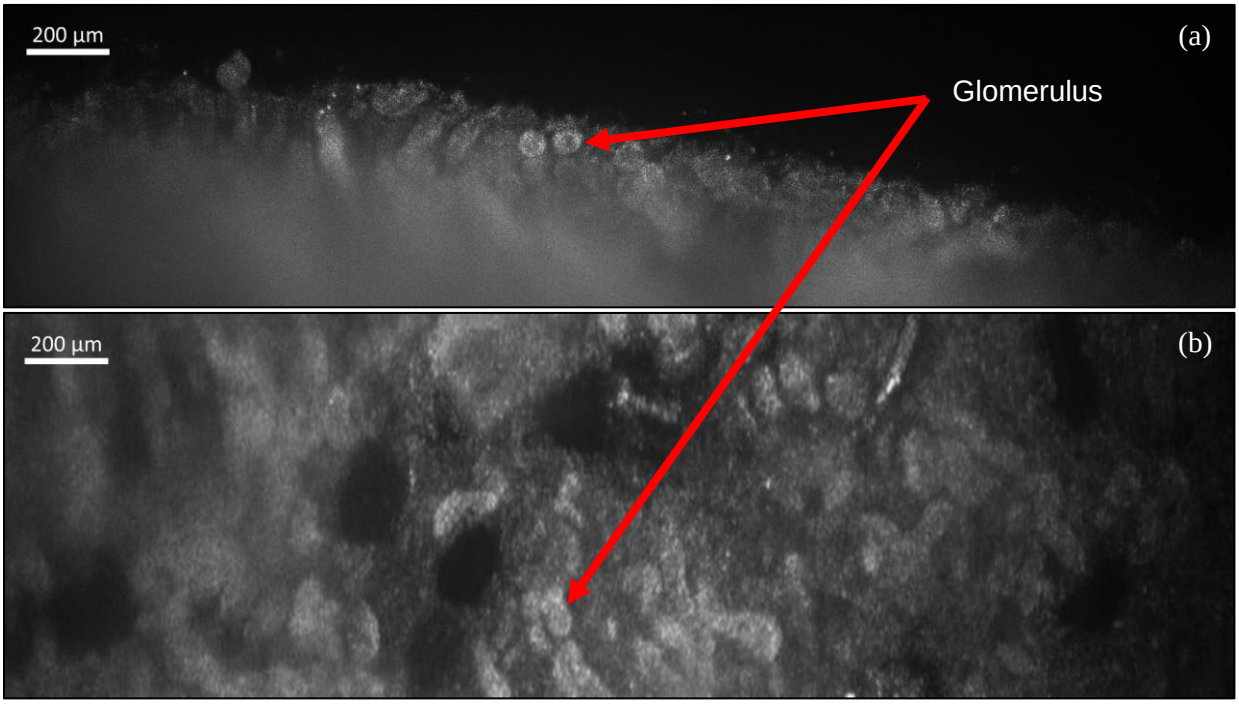

Figure 4.06 – (a) Single frame of the video acquired of swine kidney. (b) En face frame of the sheared and compressed volume matrix.

4.2.3 Skin Images

After acquiring preliminary results of both plant and animal cells, the system was used to collect data of human skin. The region that was chosen to be imaged was the forearm as it easily fits underneath our device. The results are shown below in Figure 4.07. The power onto the skin was 0.9mW for an exposure time of 4.6ms.

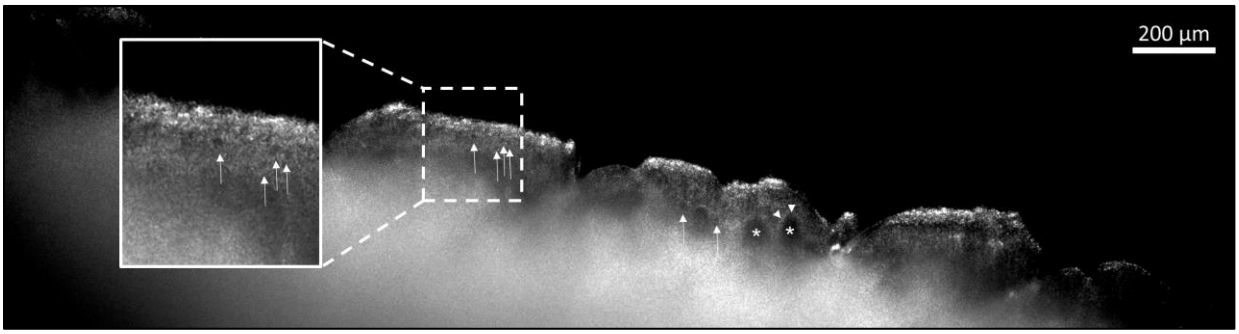

Figure 4.07 – Image of human forearm phototype 3 skin. Arrows represent keratinocytes, arrow heads represent melanocytes, and asterisks represent dermal papillae.

The cellular characteristics visualized using the light sheet microscope are similar to those acquired with reflectance confocal microscopes. Keratinocytes appear as dark nuclei surrounded by bright grainy cytoplasm. Clusters of keratinocytes are typically found in a regular honeycomb pattern unless malignancies are present which disrupts the pattern. Melanocytes appear as bright round or oval objects. Differentiating these cells typically require context from the surrounding architectural content. An example is that they are generally found surrounding the dermal papillae. Dermal papillae appear as dark round or oval areas surrounded by melanocytes and the grainy cytoplasm from keratinocytes [31]. Using these known characteristics, the three cellular features can be distinguished in the skin as shown in Figure 4.07.

4.3 Light Sheet Microscope with Visible Light Illumination Results

4.3.1 Plant Images

Similar to the infrared system, before the visible light sheet microscope was used to collect data of the skin, the system was used to image a cucumber. The results are shown below in Figure 4.08. The apparent structures are similar to the OCT images shown above in Figure 4.05. By applying the processing technique in Section 4.1, a large area en face image of the cucumber can be acquired as shown in Figure 4.09. To note, the cucumber used in Figure 4.08 and Figure 4.09 are different types of cucumbers.

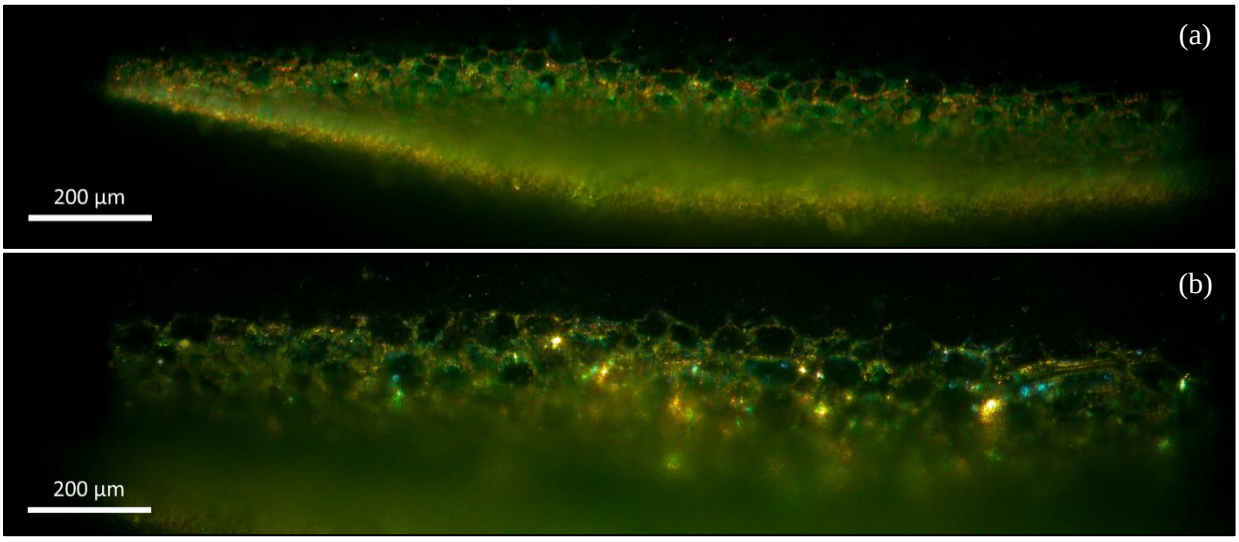

Figure 4.08 – Image of cucumber cells. (a) Near the edge. (b) Close to the center.

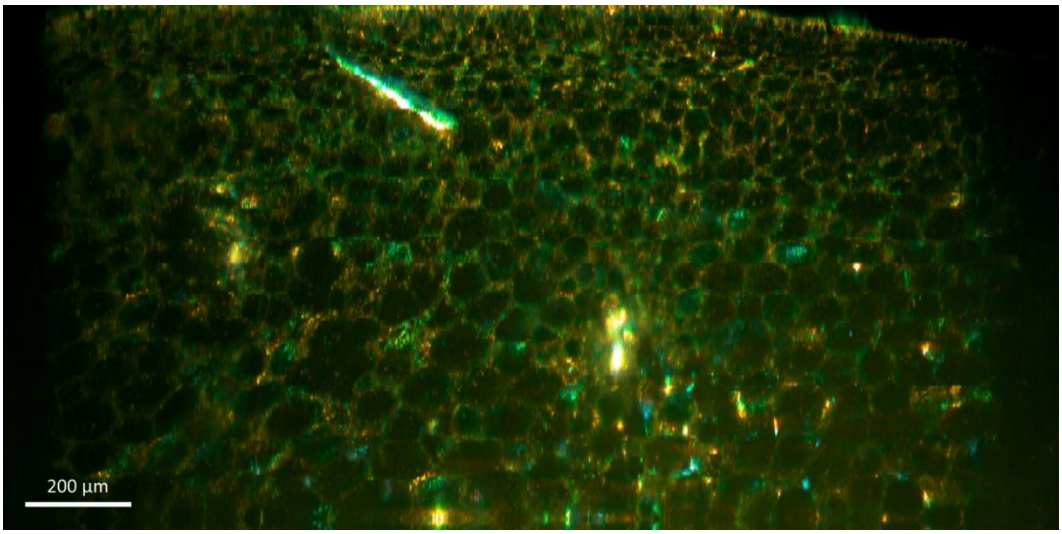

Figure 4.09 – Large area en face image of cucumber.

4.3.2 Skin Images

The results shown in Figure 4.10 is an image taken with the visible light sheet microscope. The results have yet to be evaluated by a dermatologist. However, preliminary spectral analysis was performed by separating the RGB channels as shown in Figure 4.11. When subtracting the green from the red channel and emphasizing the results onto a grayscale image as shown in Figure 4.11(a), it can be seen that red pixels tend to delineate the dermal papillae which is a characteristic of melanin. Subtracting the red from the green channel results in a negative of the green subtracted from the red channel. Green pixels therefore tend to appear inside the dermal papillae as seen in Figure 4.11(b). An interesting thing to recognize is that in the dermis, the red channel is emphasized while the green channel is missing which represents the deeper penetration depth of longer wavelengths. The composite of both Figure 4.11(a) and Figure 4.11(b) is shown in Figure 4.11(c). The impact of this preliminary analysis of the spectral characteristics of the tissue has yet to be confirmed; however, it can be seen that different parts of the skin tissue have unique responses.

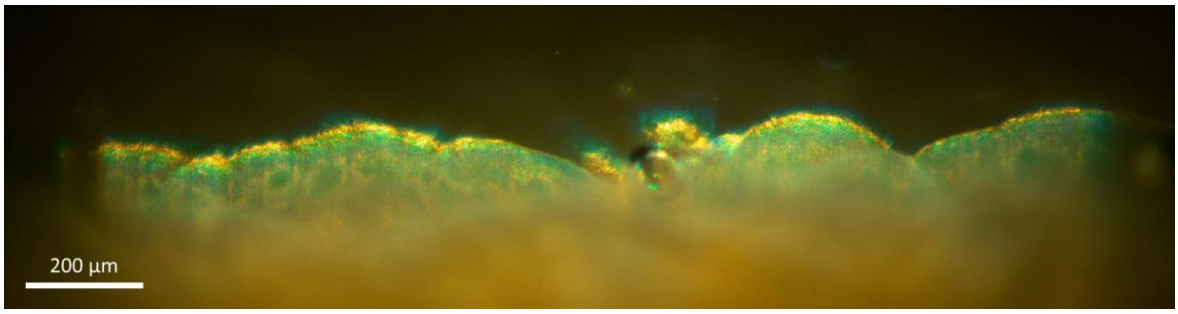

Figure 4.10 – Image of human forearm phototype 5 skin.

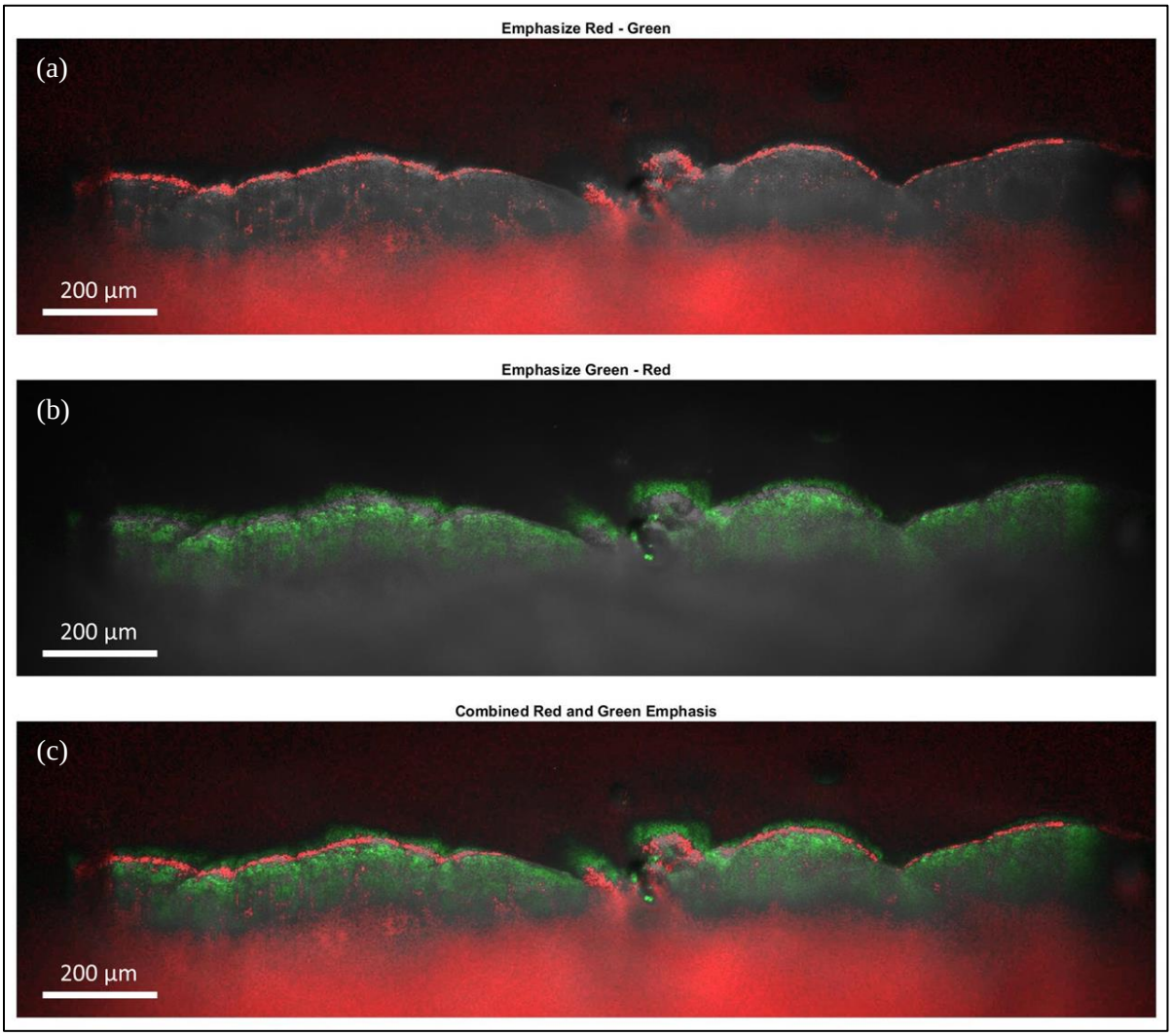

Figure 4.11 – (a) Red minus green channel emphasized onto grayscale image of Figure 4.09. (b) Similar to (a) but emphasizes green minus red channel. (c) Emphasis in (a) and (b) combined.

Chapter 05: Conclusion and Discussion

Two issues that both systems still face are speckle noise and shadowing artefacts. The method used for both systems to reduce speckle noise was to increase the bandwidth of the source. For the infrared system, by increasing the bandwidth from approximately 10nm to 44nm, the speckle contrast decreased from 80% to 18% as seen in Figure 5.01. However, this amount of speckle is still detrimental to the system as the random fluctuations can still be mistaken for cellular features. Future improvements may involve switching to a source with a larger bandwidth or less spatial coherence, or to include optics to scramble the spatial coherence to provide speckle reduction spatially and temporally.

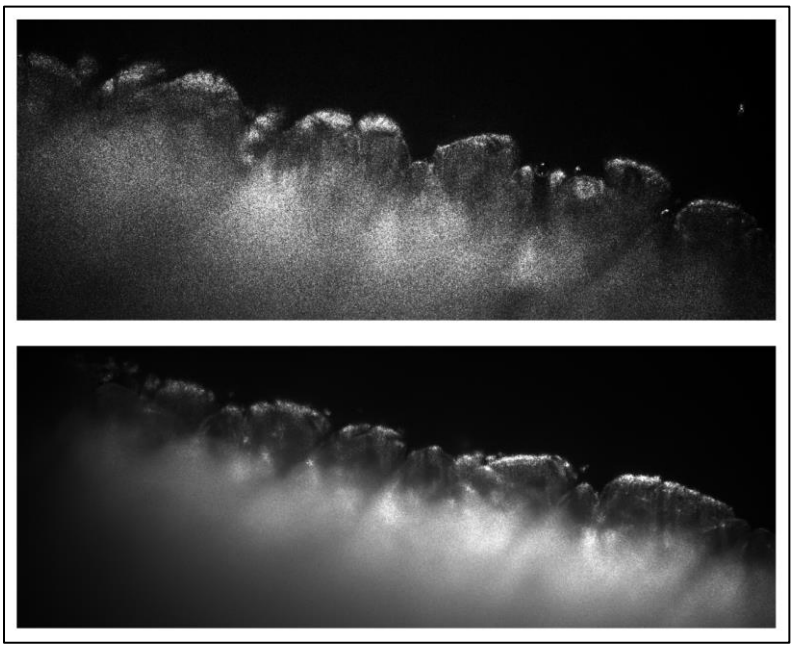

Figure 5.01 – Comparison of skin imaging results using different infrared sources. Top image used single wavelength laser diode and bottom image used SLED with a large bandwidth.

To decrease the shadowing artefacts as shown in Figure 5.02, current efforts involve modifying the optics to illuminate the sample at multiple angles simultaneously or individually. Similar to dual-sided illumination, shadow artefacts may be reduced if the sample is illuminated in multiple

directions. Additionally, the increase in illumination angles will create various speckle patterns that will average out to reduce the speckle contrast.

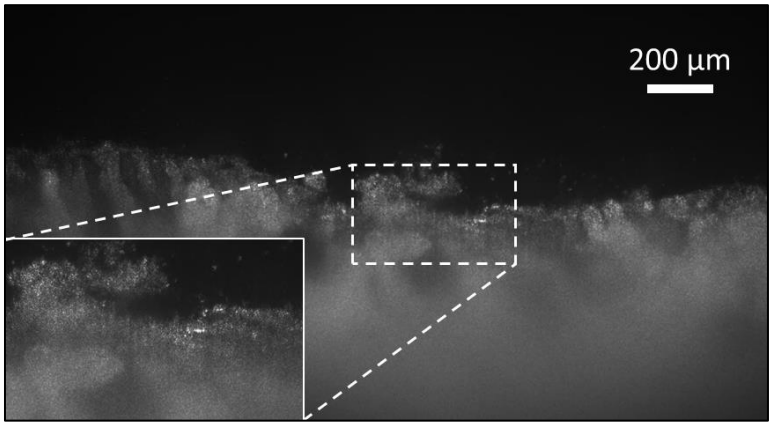

Figure 5.02 – Image from swine kidney data set displaying shadowing artefacts which appear as dark vertical lines. Shadows potentially block relevant cellular features from being illuminated.

For real time imaging, a faster acquisition rate is desired to detect the small changes in tissue structure. The current detector was chosen due to its large number of horizontal pixels which were required to image the full horizontal field of view at the Nyquist frequency. As for the full vertical field of view, the number of required pixels is significantly less as the vertical field of view is relatively small compared to the horizontal. However, the detector size is 4024 pixels by 3036 pixel which means the majority of the vertical pixels are unused. Recording and storing images this large requires a relatively significant amount of time and most of the image is undesired. To therefore speed up the acquisition rate which is currently 30 frames per second, the detector should be replaced with a detector that has a size ratio better matching the image size.

Once the system is built and tested for performance, clinical trials may begin. However, to help facilitate easier data collection, the device may be miniaturized to make the light sheet microscope portable. The current size of the system is approximately 27cm by 4.8cm by 16cm. Current efforts involve modifying the system to place the illumination and detection arm parallel to one another and bending the illumination path with a mirror. The limitation in size is due to the

current configuration using a commercial objective lens for the illumination arm to produce a high-quality beam. With a working distance of only 3.5mm, the mechanical size of the objective prevents placing the illumination objective parallel to the detection objective. The commercial objective lens will therefore be replaced with smaller optics that can be placed close to the mirror without interfering with the detection objective. After the device is miniaturize, clinical testing may start to collect data from a larger sample set to characterize the sensitivity and specificity.

References

[1] J. Thingnes, T. J. Lavelle, E. Hovig, and S. W. Omholt, "Understanding the Melanocyte Distribution in Human Epidermis: An Agent-Based Computational Model Approach," *PLoS One*, vol. 7, no. 7, p. 40377, 2012.

[2] R. Gräf, J. Rietdorf, and T. Zimmermann, "Live cell spinning disk microscopy," *Adv. Biochem. Eng. Biotechnol.*, vol. 95, no. September 2015, pp. 57–75, 2005.

[3] G. Cox and C. J. R. Sheppard, "Practical Limits of Resolution in Confocal and Non-Linear Microscopy," *Microsc. Res. Tech.*, vol. 63, pp. 18–22, 2004.

[4] R. H. Webb, "Confocal optical microscopy," 1996.

[5] C. L. Smithpeter, A. K. Dunn, A. J. Welch, and R. Richards-Kortum, "Penetration depth limits of in vivo confocal reflectance imaging," *Appl. Opt.*, vol. 37, no. 13, p. 2749, May 1998.

[6] T. Milster, "Chapter 04 Interference and Interferometry." pp. 1–64, 2017.

[7] A. L. Oldenburg, C. Xu, S. A. Boppart, and S. Member, "Spectroscopic Optical Coherence Tomography and Microscopy," *IEEE J. Sel. Top. QUANTUM Electron.*, vol. 13, no. 6, 2007.

[8] M. Choma, M. Sarunic, C. Yang, and J. Izatt, "Sensitivity advantage of swept source and Fourier domain optical coherence tomography," 2003.

[9] B. E. Bouma, S.-H. Yun, B. J. Vakoc, M. J. Suter, and G. J. Tearney, "Fourier-domain optical coherence tomography: recent advances toward clinical utility.," *Curr. Opin. Biotechnol.*, vol. 20, no. 1, pp. 111–8, Feb. 2009.

[10] J.-L. Perrot *et al.*, "Line-field confocal optical coherence tomography for high-resolution noninvasive imaging of skin tumors," *J. Biomed. Opt.*, 2018.

[11] H. G. Bezerra, M. A. Costa, G. Guagliumi, A. M. Rollins, and D. I. Simon, "Intracoronary optical coherence tomography: a comprehensive review clinical and research applications.," *JACC. Cardiovasc. Interv.*, vol. 2, no. 11, pp. 1035–46, Nov. 2009.

[12] P. J. Keller *et al.*, "Fast, high-contrast imaging of animal development with scanned light sheet–based structured-illumination microscopy," *Nat. Methods*, vol. 7, no. 8, pp. 637–642, Aug. 2010.

[13] O. E. Olarte, J. Andilla, E. J. Gualda, and P. Loza-Alvarez, "Light-sheet microscopy: a tutorial," *Adv. Opt. Photonics*, vol. 10, no. 1, pp. 111–179, 2018.

[14] C. Ash, M. Dubec, K. Donne, and T. Bashford, "Effect of wavelength and beam width on penetration in light-tissue interaction using computational methods.," *Lasers Med. Sci.*, vol. 32, no. 8, pp. 1909–1918, Nov. 2017.

[15] Z. Gajinov, M. Matić, S. Prćić, and V. Đuran, "Optical properties of the human skin," *Serbian J. Dermatology Venerol.*, vol. 2, no. 4, pp. 131–136, 2013.

[16] J. Gill, “Creating an Exotic New Form of Light with Simple Optical Elements,” 2014.

[17] A. Aadhi, N. A. Chaitanya, M. V. Jabir, P. Vaity, R. P. Singh, and G. K. Samanta, “Airy beam optical parametric oscillator,” *Sci. Rep.*, vol. 6, no. 1, p. 25245, Jul. 2016.

[18] D. Mcgloin and K. Dholakia, “Bessel beams: Diffraction in a new light,” *Contemp. Phys.*, vol. 46, no. 1, pp. 15–28, 2005.

[19] J. Huisken and D. Y. R. Stainier, “Selective plane illumination microscopy techniques in developmental biology,” *Development*, vol. 136, no. 12, pp. 1963–1975, Jun. 2009.

[20] B. Schmid *et al.*, “High-speed panoramic light-sheet microscopy reveals global endodermal cell dynamics,” *Nat. Commun.*, vol. 4, no. 1, p. 2207, Dec. 2013.

[21] C. Glazowski and M. Rajadhyaksha, “Optimal detection pinhole for lowering speckle noise while maintaining adequate optical sectioning in confocal reflectance microscopes.,” *J. Biomed. Opt.*, vol. 17, no. 8, p. 085001, Aug. 2012.

[22] V. Bianco *et al.*, “Strategies for reducing speckle noise in digital holography,” *Light Sci. Appl.*, vol. 7, no. 1, p. 48, Dec. 2018.

[23] M. Esmaeili, A. M. Dehnavi, H. Rabbani, and F. Hajizadeh, “Speckle Noise Reduction in Optical Coherence Tomography Using Two-dimensional Curvelet-based Dictionary Learning,” *J. Med. Signals Sens.*, vol. 7, no. 2, pp. 86–91, 2017.

[24] M. Sarode and P. Deshmukh, “Reduction of Speckle Noise and Image Enhancement of Images Using Filtering Technique,” *Int. J. Adv. Technol.*, vol. 2, no. 1, pp. 30–38, 2011.

[25] T. Stangner, H. Zhang, T. Dahlberg, K. Wiklund, and M. Andersson, “Step-by-step guide to reduce spatial coherence of laser light using a rotating ground glass diffuser,” *Appl. Opt.*, vol. 56, no. 19, p. 5427, Jul. 2017.

[26] H. Farrokhi *et al.*, “High-brightness laser imaging with tunable speckle reduction enabled by electroactive micro-optic diffusers.,” *Sci. Rep.*, vol. 7, no. 1, p. 15318, Nov. 2017.

[27] M. N. Akram, Z. Tong, G. Ouyang, X. Chen, and V. Kartashov, “Laser speckle reduction due to spatial and angular diversity introduced by fast scanning micromirror,” *Appl. Opt.*, vol. 49, no. 17, p. 3297, Jun. 2010.

[28] T. Milster, “Chapter 06 Coherence and Fringe Localization.” pp. 1–88, 2018.

[29] A. K. Dunn, “Laser speckle contrast imaging of cerebral blood flow.,” *Ann. Biomed. Eng.*, vol. 40, no. 2, pp. 367–77, Feb. 2012.

[30] S. Marschall *et al.*, “Fourier domain mode-locked swept source at 1050 nm based on a tapered amplifier,” *Opt. Express*, vol. 18, no. 15, p. 15820, Jul. 2010.

[31] A. Levine and O. Markowitz, “Introduction to reflectance confocal microscopy and its use in clinical practice,” *JAAD Case Reports*, vol. 4, no. 10, p. 1014, 2018.